Single-step hydrogen production from NH$_3$, CH$_4$, and biogas in stacked proton ceramic reactors

Authors: Daniel Clark[1], Harald Malerød-Fjeld[1], Michael Budd[1], Irene Yuste-Tirados[1,2], Dustin Beeaff[1], Simen Aamodt[1], Kevin Nguyen[1], Luca Ansaloni[3], Thijs Peters[3], Per K. Vestre[1], Dimitrios K. Pappas[1], María I. Valls[4], Sonia Remiro-Buenamañana[4], Truls Norby[2], Tor S. Bjørheim[1], Jose M. Serra[4*], Christian Kjølseth[1*]

Affiliations:

[1]CoorsTek Membrane Sciences AS; 0349 Oslo, Norway.

[2]Department of Chemistry, Centre for Materials Science and Nanotechnology, University of Oslo; 0316 Oslo, Norway.

[3]Department of Sustainable Energy Technology, SINTEF Industry; 0314 Oslo, Norway.

[4]Instituto de Tecnologia Quimica, Consejo Superior de Investigaciones Científicas-Universitat Politecnica de Valencia; 46022 Valencia, Spain.

*Corresponding authors. Email: jmserra@itq.upv.es; ckjolseth@coorstek.com

Abstract: Proton ceramic reactors offer efficient extraction of hydrogen from NH$_3$, CH$_4$, and biogas by coupling endothermic reforming reactions with heat from electrochemical gas separation and compression. Preserving this efficiency in scale-up from cell to stack level poses challenges to the distribution of heat and gas flows and electric current throughout a robust functional design. We herein demonstrate a 36-cell well-balanced reactor stack enabled by a novel interconnect that achieves complete conversion of CH$_4$ with >99% recovery to pressurized H$_2$ leaving a concentrated stream of CO$_2$. Comparable cell performance is achieved also with NH$_3$ and operation was confirmed at pressures as high as 141 bar. The stacking of proton ceramic reactors into practical thermo-electrochemical devices demonstrates their potential in efficient hydrogen production.

One-Sentence Summary: Proton ceramic electrochemical stack scales up energy-efficient on-site production of hydrogen from ammonia and methane streams.

Main Text:

Hydrogen (H_2) can be produced from methane-rich streams through steam reforming and water-gas shift (SMR+WGS, $CH_4 + 2H_2O = CO_2 + 4H_2$, $\Delta_r H° = 164.7$ kJ/mol) or from the emerging carbon-free H_2-carrier NH_3 through ammonia dehydrogenation (ADH, $NH_3 = 1/2N_2 + 3/2H_2$, $\Delta_r H° = 45.9$ kJ/mol) (*1-3*). In a conventional multi-stage hydrogen production process, fuel combustion generates the heat for these endothermic reactions while separation and compression are handled downstream by pressure-swing adsorption and mechanical compressors. Efficiencies typically improve with scale, favoring large centralized processes over distributed H_2 production for energy-carrier applications (*4*). H_2 can also be separated and compressed electrochemically with proton ceramic membranes such as Y-doped $BaZrO_3$-$BaCeO_3$ solid solutions (BZCY) that are functional and stable over a wide range of temperatures (300 to 800°C) and chemical environments (*5-10*). Proton ceramic electrochemical reactors (PCERs) extract pure H_2 from gas mixtures by electrolytically pumping protons across the membrane (Fig. 1A). They offer process intensification (*9*) by integrating reactions such as SMR+WGS or ADH with H_2 separation and compression, high energy efficiencies by supplying heat electrically (*11*), and reduced CO_2 emissions when that electricity is renewable (*12*).

As for any compression process, the work associated with electrochemical H_2 compression is minimized by operating isothermally (*13*). In a continuous-flow type PCER, the compression ratio and associated entropy difference of H_2 across the membrane increase with the extent of separation along the reactor (Fig. 1B and fig. S1). This entropy difference is expelled as heat ($Q = T\Delta S$) during the compression process which, if left unbalanced, leads to gradually increasing temperature along the reactor, and in turn larger electric energy consumption per kg of compressed H_2 (Fig. 1B). Isothermal operation can be achieved by locally balancing this heat evolution with a reversible heat sink such as an endothermic chemical reaction (fig. S2) (*9*). However, matching the spatial distribution of heat from compression with the extent of chemical reactions throughout a stacked reactor poses one of the main hurdles in scaling PCERs from laboratory to commercial deployment. Furthermore, scaled reactors with efficient current distribution have been hindered by the lack of interconnect materials with high electrical conductivity and chemical stability up to 800 °C that match the low thermal expansion coefficient (8×10^{-6} K^{-1}) of the preferred proton conductor BZCY.

We show an optimized reactor architecture aided by multiphysics simulations and a new metal/glass-ceramic composite interconnect (IC) that enables deployable modular PCER stacks that retain the energy efficiencies and H_2 recoveries of single cells (*9*), while achieving a 36-fold increased H_2 production capacity.
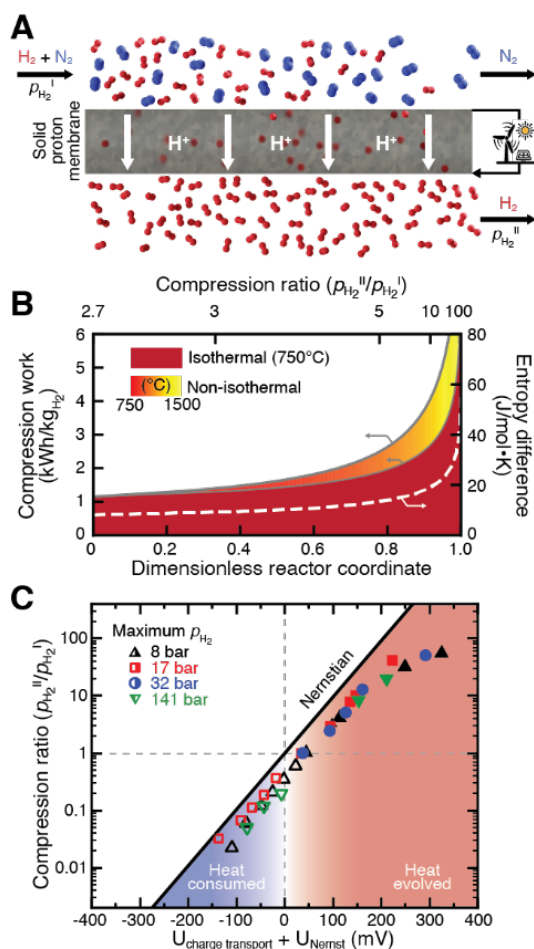
Fig. 1. Hydrogen separation and compression using PCERs. (**A**) Schematic of electrochemical H_2 separation and compression from a H_2+N_2 mixture in continuous-flow type PCER. (**B**) Compression work for isothermal and non-isothermal H_2 separation from a N_2+H_2 mixture. The local compression ratio for H_2 and associated entropy difference $\left(\Delta S(x) = R\ln\left(p_{H_2}^{II}/p_{H_2}^{I}(x)\right)\right)$ increase along the reactor coordinate, which leads to an increase in compression work and heat expelled from the compression process ($w_{el}(x) = Q(x) = T\Delta S(x)$). If left unbalanced, this heat increases the temperature throughout the reactor, particularly in the latter parts, resulting in higher compression work than for ideal isothermal operation. (**C**) Compression ratio as a function of $U_{charge\ transfer} + U_{Nernst}$ at 750°C for a maximum pH_2 from 8 to 141 bar measured using representative PCER single cells (fig. S3) at $i = 50$ mA/cm^2, illustrating the different operation modes. The compression ratio range was covered by adjusting the minimum pH_2 as well as gas flows to ensure low degree of H_2 extraction/dilution. The blue region consumes while the red region evolves heat.

Our PCER can separate H_2 by decompression while recovering electric energy, or by compression through supply of electric energy (Fig. 1C) at pressures up to 141 bar, illustrating the range of compression ratios and associated cell voltages that can be achieved throughout the PCER stack length. The PCER stack is a series of 6 barrels each with 6 single cells connected electrically in parallel (Fig. 2A and fig. S4A) using novel Ni-based glass-ceramic composite ICs (*14*). A conductive washer of the same material is placed between the end of each membrane segment and the IC plate (Figs. 2E and F). Unlike pure metals with higher thermal expansions, such as Ni or Cu that are prone to loss of electric contact during thermal cycling (fig. S5A), our glass/Ni- composite washer deforms during sealing to

3

maximize surface contact area and minimize joint resistance. The novel washer is applied in a partially heat-treated condition, as a sintered glass/Ni-composite, rather than a fully heat-treated glass-ceramic/Ni composite. This allows the washer to deform under the load applied during the heating phase of the sealing cycle by virtue of viscous flow in the glassy matrix phase in the washer, thereby making intimate surface contact with both components. The glassy matrix phase wets the ceramic phases in both the tubular cell support and the IC and produces a mechanically-strong bond. By the end of the sealing cycle, the glassy matrix phase in the washer crystallizes to produce a matched expansion glass-ceramic/Ni composite bridge which retains excellent electrical continuity between the cell and the IC throughout subsequent thermal cycling. The adopted IC material exhibits conductivities >2500 S/cm at 750°C and thermal expansion coefficients in a close-to-perfect match with the thermal expansion of the membrane support (Fig. 2D, fig. S5B and table S1), ensuring efficient current distribution throughout the stack and mechanical robustness. The IC is chemically stable under reducing and CO_2-rich atmospheres, but can also be fitted with more oxidation-resistant metallic components such as Ag for operation under oxidizing conditions (fig. S5, C to E). The absence of chromium furthermore eliminates degradation issues related to formation of resistive Cr_2O_3 scales or evaporation of volatile chromium species during long-term operation at high temperatures.
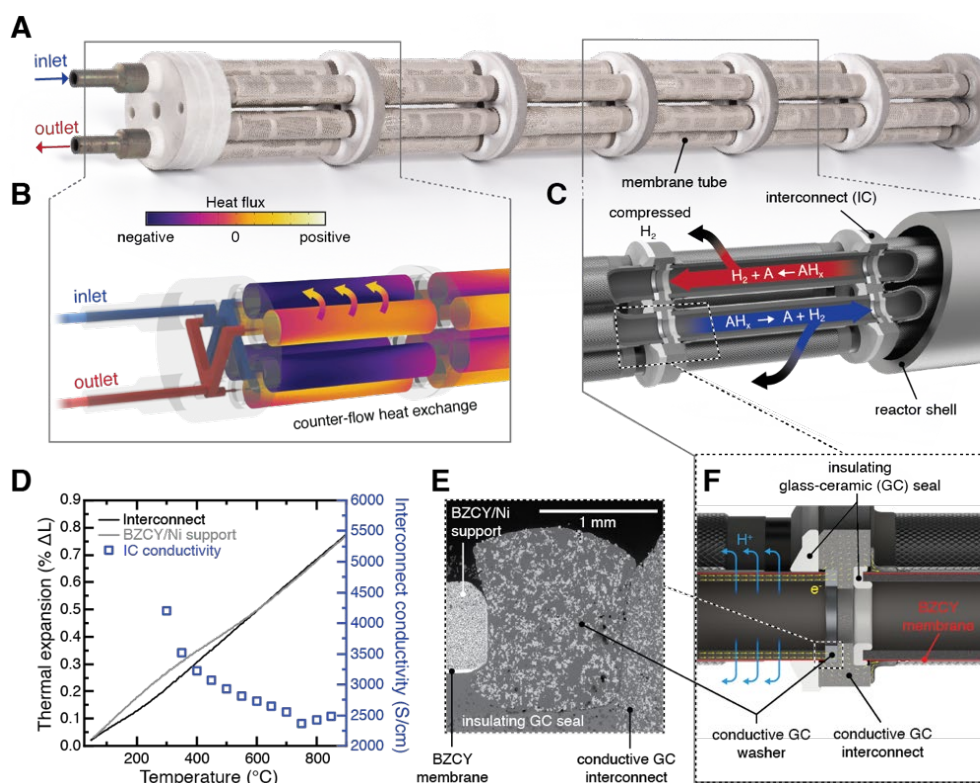

Fig. 2. PCER stack for electrochemical hydrogen production. (A) PCER stack (dimensions: height 43 cm, diameter 4 cm). **(B)** Schematic of microthermal heat integration with outward heat flux from the cells. **(C)** Schematic of U-bend type gas flow of the generic molecule AH_x reacting to form H_2 which is electrochemically extracted as H^+ through the membrane and recovered as compressed H_2 in the outer chamber. **(D)** Thermal expansion upon cooling of the BZCY/Ni support and the IC, and IC electrical conductivity as a function of temperature. **(E)** Scanning electron micrograph cross-section of the interface between the BZCY/Ni support and IC, connected by a conductive glass-ceramic washer. **(F)** Schematics of IC and washer assembly.

During operation, individual cells will be net endo- or exothermic depending on the degree of reaction and H_2 separation and compression throughout the stack length (Fig. 1C and Fig. 2B), necessitating internal heat exchange. To guide the optimal design of the stack, we adopted a three-dimensional multiphysics model integrating coupled gas flows, heat transfer, current distribution and reaction kinetics for SMR+WGS and ADH that captures the behavior of the stack from single cell to stack level (*14*). Our stack is designed with a U-bend type gas flow pattern achieved by a manifold that distributes the incoming gas to three of the six gas channels in the stack while combining the three corresponding exhaust streams. As illustrated for SMR+WGS (Fig. 3), this lowers temperature gradients and Nernst potentials through the stack compared to an axial type reactor (Fig. 3, A and B, and fig. S5), which in turn lowers the electricity consumption per kg produced hydrogen. Coupled with the high performing IC, our design allows currents (i.e. hydrogen fluxes) to self-regulate according to the local Nernst voltage (fig. S6). For anhydrous ADH, SMR+WGS and biogas this is particularly evident in the first barrels of the stack due to the fast reaction kinetics which concentrates the reaction to the initial parts of the stack (figs. S7 to S9). The slower reaction kinetics of aqueous ADH distributes the reaction over a larger portion of the stack which in turn leads to more uniform temperature profile (fig. S10).
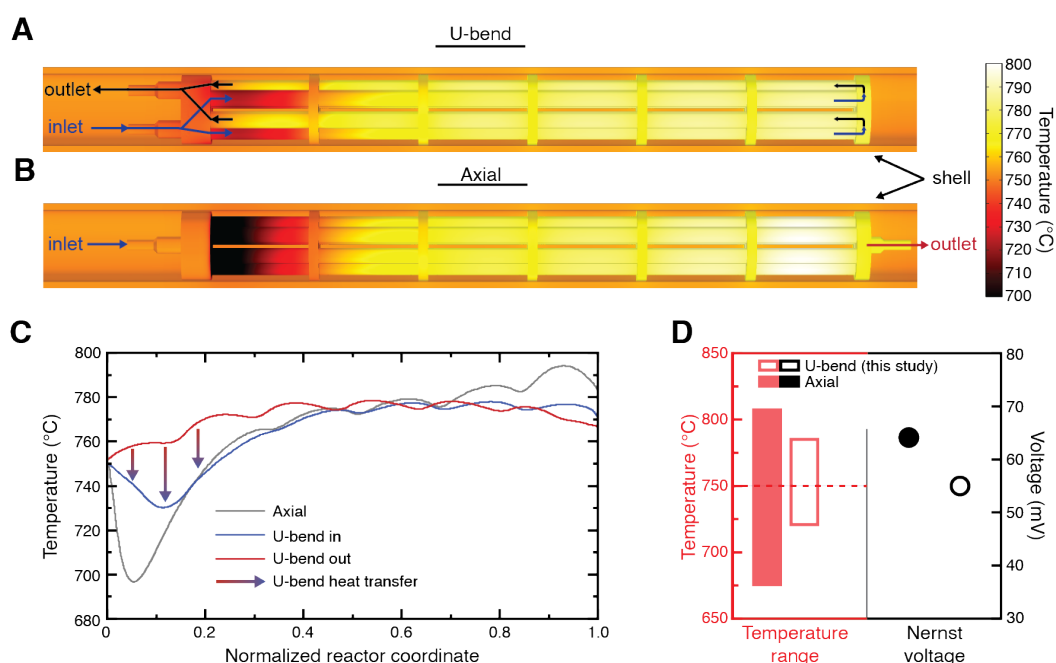

Fig. 3. Multiphysics simulations of PCER stack thermally-balanced operation. Multiphysics simulations for a stack operating at 750°C external temperature with 20 bar total pressure on both sides of the membrane, mean current density of 0.60 A/cm². Feed: 28.6% CH_4 (0.597 NL/min), 71.4% H_2O. Sweep: H_2O (0.18 g/min). (**A**) Simulated temperature fields in a U-bend PCER stack architecture, indicating also the gas inlet and outlet flow distribution. (**B**) Simulated temperature fields in an axial PCER stack architecture. (**C**) Centerline temperature profiles on the reforming side in the axial and U-bend architecture as function of reactor length. The thermal balancing by heat transfer between first cell (net endothermic) and last cell (net exothermic) for U-bend PCER is illustrated by vertical arrows. (**D**) Comparison of simulated temperature range and mean Nernst voltage in U-bend and axial stack architectures.

To experimentally demonstrate integration of reactions beyond SMR+WGS in our PCER stack (*9*), single cells were operated with NH_3 in both anhydrous and aqueous form (*14*). The cells achieve >95% conversion of NH_3 even at open-circuit conditions (Fig. 4A) and near

100% conversions at high H_2 recoveries thus leaving an effluent stream virtually free of residual NH_3. The cells demonstrate comparable performance with anhydrous and aqueous NH_3, CH_4 and biogas, retaining near faradaic behavior to above 1 A/cm^2 (fig. S11), reflecting the catalytic versatility of the porous Ni-BZCY support. With CH_4, the single cells even achieved >90% faradaic efficiency up to 7.4 A/cm^2 (corresponding to a H_2 flux of 47 mL/(min cm^2) (fig. S12) thus doubling the H_2 production capacity to-date with these materials (*9*).
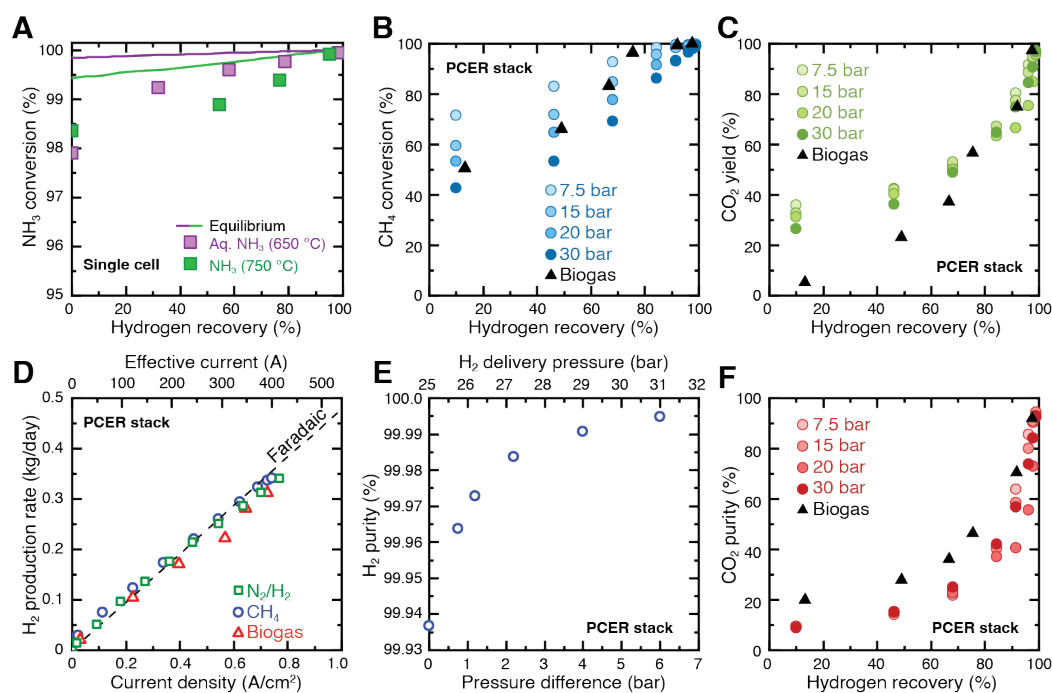

Fig. 4. PCER single cell and stack performance. (**A**) NH_3 conversion as a function of hydrogen recovery, measured on a representative single cell (fig S3) at 650°C and 10 bar (pNH_3 = 7.25 and pH_2O = 2.75 bar); and aqueous NH_3 at 750°C and 10 bar (pNH_3 = 3.1 bar, pH_2O = 5.8 bar and p_{inert} = 1.1 bar); green and purple lines show the equilibrium conversion for NH_3 and aq. NH_3, respectively. (**B**) and (**C**) CH_4 conversion and yield of CO_2 vs. H_2 recovery, respectively, of PCER stack at 750°C. (**D**) Hydrogen production rate as a function of applied current density for the stack with N_2/H_2 mix simulating complete NH_3 decomposition (750°C, 10 bar), methane (800°C, 15 bar, S/C = 2.5) and biogas (750°C, 20 bar, S/C = 2.5). Effective current is calculated by *current density* x *PCER stack area* (36 × 15 cm^2) and applied current by *effective current*/6 due to the series and parallel electric architecture. (**E**) Hydrogen purity (dry basis) vs. hydrogen delivery pressure and differential pressure across the membranes, and (**F**) CO_2 purity vs. hydrogen recovery, for SMR+WGS in the stack at 750°C. Reforming side pressure = 25 bar, hydrogen side pressure 25–31 bar. Current density = 0.69 A/cm^2.

The 36-cell PCER stack achieves nearly full CH_4 conversion and high H_2 recoveries (>99%, Fig. 4 and fig. S13) for CH_4 and biogas, enabling complete equilibrium shift and a CO_2 rich effluent stream for facile carbon capture. The series and parallel design of the stack facilitates an effective aggregated current of up to 400 A (i > 0.73 A/cm^2) with a H_2 production rate up to 0.34 kg/day from CH_4, 0.31 kg/day from biogas, and 0.34 kg/day from simulated fully decomposed NH_3 stream (Fig. 4D). Both production rate (10x) and active area (>6x) greatly surpass those of any reported for proton ceramic applications (*9, 15*). We furthermore demonstrate H_2 compression to 31 bar with a purity of 99.995% (Fig. 4E) facilitated for

6

additional compression and use. The PCER stack shows promising stability, retaining a H_2 production rate of 2 NL/min after 1400 hours of operation (fig. S14).

System modelling (*14*) of a 1 ton/day distributed H_2 production plant adopting our PCER stack (figs. S15 to S21) reveals that efficiencies of 91% for CH_4 and as high as 95% for anhydrous NH_3 can be achieved by virtue of microthermal integration and downstream heat recovery. Furthermore, the PCER delivers a concentrated and pressurized stream of CO_2 when operated on methane or biogas (Fig. 4F) that can be purified and liquefied by cryogenic distillation, eliminating the need for complex downstream absorption-based CO_2 capture.

The high degree of process intensification achieved by our PCER stacks enables a fuel-flexible energy-efficient alternative to established technologies for distributed H_2 production. Using a California 2020 electric grid carbon intensity scenario (82.92 $g_{CO2}/MJ_{elec,}$. see table S2 for references) H_2 production with PCERs using CH_4 as fuel would operate at lower emissions (75.7 vs. 124.1 g_{CO2}/MJ_{H2}) than water electrolysis powered by grid electricity, even without CO_2 sequestration. With decarbonization of the electric grid, CO_2 sequestration is required for methane reforming to remain competitive with water electrolysis. In a California 2050 grid scenario, PCERs can produce H_2 from CH_4 with lower CO_2-emissions than water electrolysis (18.7 vs. 26.2 g_{CO2}/MJ_{H2}) when CO_2 is sequestrated. PCERs operated on biogas even offer H_2 production with net-negative carbon emission, as CH_4 from a biogenic process is considered carbon-neutral. Calculated scenarios have used the CA GREET model (*16*) which includes fugitive methane emissions from natural gas production that can be significant (*17*).

To illustrate the practical implications of the PCER technology, comparable well-to-wheel emissions for battery electric vehicles (BEVs), internal combustion engines (ICEs) with diesel fuel, and H_2 fuel cell electric vehicles (FCEVs) are provided in fig. S22 with sensitivity to electric grid carbon intensity shown in fig. S23. In the California 2050 scenario, the emissions of FCEVs (14.6 g_{CO2}/km) using H_2 produced from CH_4 with PCERs including CO_2 sequestration are 90% lower than those of ICE with diesel fuel (145.4 g_{CO2}/km) and 26% lower than FCEVs using H_2 from grid-powered water electrolysis (19.8 g_{CO2}/km). NH_3-based H_2 can offer reduced emissions compared to on-site electrolysis for a wide range of electric grid carbon intensities, making FCEVs fueled with NH_3-based H_2 directly comparable to BEVs in terms of CO_2 emissions (6.3 g_{CO2}/km, a reduction of 21% compared to BEV in the California 2050 scenario). Here, NH_3 is assumed produced at off-site locations with favorable renewable energy resources and transported as a liquid to the fueling station where efficient ADH and separation to H_2 takes place using the PCER technology.

The growth of a new energy technology can be limited by access to raw materials. A detailed examination of raw materials' usage of the PCER stack (fig. S24) shows it is comprised of non-precious, earth-abundant materials, suggesting no material availability setbacks for scaling.

Competing interests: DC, HMF, MB, IYT, DB, SA, KN, DKP, TSB, and CK are employed by CoorsTek Membrane Sciences (CTMS). CTMS have filed relevant patent application PCT/EP2017/076340. TN is a member of the CTMS board. IYT PhD studies at the University of Oslo (UiO) is partially funded by CTMS. All other authors declare that they have no competing interests.

Data and materials availability: All data are available in the main text or the supplementary materials. Experimental data is available online at ftp://itqrepositorio.itq.upv.es/pub/.

Supplementary Materials

Materials and Methods

Figs. S1 to S30

Tables S1 to S5

References (*18-42*)

References and notes

1. R. F. Service, New recipe produces ammonia from air, water, and sunlight. *Science* **345**, 610-610 (2014).
2. S. T. Wismann *et al.*, Electrified methane reforming: A compact approach to greener industrial hydrogen production. *Science* **759**, 756-759 (2019).
3. I. Staffell *et al.*, The role of hydrogen and fuel cells in the global energy system. *Energy Environ. Sci.* **12**, 463-491 (2019).
4. G. Grashoff, C. Pilkington, C. Corti, The purification of hydrogen. *Platinum Met. Rev.***27**, 157-169 (1983).
5. J. M. Serra, Reversible electrochemical cells: Electrifying chemistry with protonic cells. *Nat. Energy* **4**, 178-179 (2019).
6. S. Choi, T. C. Davenport, S. M. Haile, Protonic ceramic electrochemical cells for hydrogen production and electricity generation: exceptional reversibility, stability, and demonstrated faradaic efficiency. *Energy Environ. Sci.* **12**, 206-215 (2019).
7. C. C. Duan *et al.*, Highly durable, coking and sulfur tolerant, fuel-flexible protonic ceramic fuel cells. *Nature* **557**, 217-222 (2018).
8. C. C. Duan *et al.*, Readily processed protonic ceramic fuel cells with high performance at low temperatures. *Science* **349**, 1321-1326 (2015).
9. H. Malerod-Fjeld *et al.*, Thermo-electrochemical production of compressed hydrogen from methane with near-zero energy loss. *Nat. Energy* **2**, 923-931 (2017).
10. H. An *et al.*, A 5×5 cm^2 protonic ceramic fuel cell with a power density of 1.3 W cm–2 at 600 °C. *Nat. Energy* **3**, 870-875 (2018).
11. S. T. Wismann *et al.*, Electrified methane reforming: A compact approach to greener industrial hydrogen production. *Science* **364**, 756-759 (2019).
12. J. L. Barton, Electrification of the chemical industry. *Science* **368**, 1181 (2020).
13. B. L. Kee *et al.*, Thermodynamic Insights for Electrochemical Hydrogen Compression with Proton-Conducting Membranes. *Membranes (Basel)* **9**, 77 (2019).
14. Materials and methods are available as supplementary.
15. R. J. Braun *et al.*, Development of kW-Scale Protonic Ceramic Fuel Cells and Systems. *ECS Transactions* **91**, 997-1008 (2019).
16. California Air Resources Board, "CA-GREET3.0 Lookup Table Pathways - Technical Support Documentation," (2018).
17. R. W. Howarth, M. Z. Jacobson, How green is blue hydrogen? *Energy Science & Engineering* **9,** 1676-1687 (2021).

Science

AAAS

Supplementary Materials for

Single-step hydrogen production from CH$_4$, biogas, and NH$_3$ in stacked proton ceramic reactors

Daniel Clark, Harald Malerød-Fjeld, Michael Budd, Irene Yuste-Tirados, Dustin Beeaff, Simen Aamodt, Kevin Nguyen, Luca Ansaloni, Thijs Peters, Per K. Vestre, Dimitrios K. Pappas, María I. Valls, Sonia Remiro-Buenamañana, Truls Norby, Tor S. Bjørheim, Jose M. Serra, Christian Kjølseth

Correspondence to: jmserra@itq.upv.es; ckjolseth@coorstek.com

This PDF file includes:

Materials and Methods

Fabrication of ceramic cells

Tubular membrane cells were prepared by co-sintering of a coated, extruded substrate. The extrudate consisted of a mixture of ceramic powders and an aqueous binder system of methylcellulose (Methocel E10M, DuPont), starch (Redisol, Tate & Lyle), and polyethylene glycol as rheology modifier (PEG400, Sigma Aldrich). The ceramic component of the extrudate was a blend of 60 wt.% NiO (IP Grade, Sumitomo) and 40 wt.% of precursor powders. The precursor powder was a mixture of $BaSO_4$ (Blanc Fixe N, Solvay), CeO_2 (American Elements), ZrO_2 (AMR) and Y_2O_3 (HJD International), the last of these in molar ratios to yield $BaZr_{0.7}Ce_{0.2}Y_{0.1}O_{3-\delta}$ (BZCY72) on decomposition and reaction. All powders, except nickel oxide, were first milled to a nominal particle size of 0.3 μm. The nickel oxide was used as-received with a particle size of 1 μm.

After extrusion and drying, the green substrate was coated with a slurry consisting of the precursors, methyl methacrylate binder (Elvacite 2927, Mitsubishi Chemical), pentyl acetate organic solvent (Sigma Aldrich) and terpineol as a rheological additive (Sigma Aldrich) using an automated spray-coater (Max-800, Ultrasonic Systems). The stoichiometry of the precursors used for the coating was adjusted to produce $BaZr_{0.8}Ce_{0.1}Y_{0.1}O_{3-\delta}$ (BZCY81) on decomposition. The outer electrode was applied by dip-coating the two-layered green tube in a slurry containing a mixture of 40 to 50 wt.% ceramic powders and the aforementioned aqueous binder system. The composition of the powder mixture was otherwise identical to that used to fabricate the substrate. The three-layered green ceramic tubes were then sintered at 1610°C for 15 hours to full density in a muffle furnace. Subsequent reduction of the nickel oxide component of the substrate was done at 1000°C for 24 h in a flow of 5% H_2 balanced with Ar. This resulted in an anode support with an open porosity of 26 vol.% as measured using the Archimedes method and corroborated with area analysis of polished cross sectioned samples. The dense electrolyte membrane thickness was 25 to 30 μm.

Metal/glass-ceramic composite interconnects

The PCER stack interconnects were made of conductive glass-ceramic/Ni composites with coefficient of thermal expansion (CTE) tailored to match that of the BZCY/Ni support (CTE$_{25-1000 °C}$ ~8.4 x 10^{-6}/K). This relatively low CTE required the use of a low expansion glass-ceramic matrix (CTE <7 x 10^{-6}/K), which, combined with the higher expansion nickel phase produced the desired composite expansion. A $CaO-MgO-Al_2O_3-SiO_2$ based glass-ceramic matrix was used in this case in combination with nickel, but other glass-ceramic systems and other metals can be used depending on which CTE range needs to be covered and the required level of electrical conductivity. Glass precursors based on alkaline-earth silicates or alkaline-earth alumino-silicates have been shown to be suitable for the fabrication of conductive glass-ceramic/metal composites incorporating Ni, Cu or Ag as the conductive phase. The main requirement is that the glass-ceramic precursor powder exhibits good sintering characteristics and can be more or less fully crystallized within the temperature limit of thermal processing of the metallic phase. For instance, $CaO-MgO-Al_2O_3-SiO_2$ based materials are favored for fabrication of the lower CTE composite materials (<9 x 10^{-6}/K), $CaO-MgO-SiO_2$ compositions for composites with intermediate CTEs (9–12 x 10^{-6}/K), and $BaO-MgO-SiO_2$ compositions for higher CTE metal/glass-ceramic composites (>12 x 10^{-6}/K). The precursor glasses were melted in a zirconia grain stabilized platinum (ZGS-Pt) crucible at temperatures in the range 1450–1600°C, using high purity raw materials (oxides and carbonates). The homogenized melts were quenched in cold water to produce frit, which was dried and subsequently milled to produce powders with an average particle size of 10–20 μm.

Fabrication of metal/glass-ceramic interconnects (ICs)

The metal/glass-ceramic composite interconnect materials were produced by co-sintering of intimate mixtures of glass-ceramic precursor and metal powder particles and the subsequent crystallization of the glass-ceramic precursor phase at a temperature of 950–1050°C (Cu/GC and Ni/GC materials) or 900–940 °C (Ag/GC materials) to form the metal/glass-ceramic composite. Commercially available metal powders were used in the fabrication of the composites. The copper and nickel were flame sprayed powders from Sandvik Osprey Ltd. with particles sizes of <22 µm and <32 µm respectively. The silver powder was grade AGP-V0180-4 from DODUCO Contacts and Refining GmbH, with an average grain size of 15–35 µm. The selected precursor glass and metal powders were well mixed in the required proportions (35–55 wt.% glass precursor/65–45 wt.% metal). Binder solution was mixed in (2% solution of QPAC-40—Empower Materials Inc.—in 2-butanone). After drying, the powder/binder mix was crushed and sieved (<125 µm). The powder mix with binder was uniaxially pressed (80 MPa) in a cylindrical die. The pressed pellets were heated at 2 K/min to 400°C and subsequently at 3 K/min to the crystallization temperature of the glass-ceramic matrix material. The materials were held at the crystallization temperature for 1–2 hours. Sintering occurred during heating to the crystallization temperature. The Ni-GC and Cu-GC composites were heat-treated in an 5% H_2 (bal. Ar) mixture, and the Ag-GC composites were sintered in air. The coefficients of thermal expansion (CTEs) range from 7 to 16 ppm/K, depending on the chosen glass-ceramic system, with electrical conductivities in the range 100–20,000 S/cm. The composites have good stability in high-pressure steam environments as well as a wide pO_2 tolerance range ($10^{-20} < pO_2 < 10$ bar), depending on the metal of choice. The ICs are chromium-free, thereby eliminating degradation issues related to formation of resistive Cr_2O_3 scales or electrode degradation due to evaporation of volatile chromium species during long term operation at high temperatures (*18*). See fig. S5 and table S1 for IC architecture and comparison with other IC materials.

Single-segment representative cells

Single-segment cells, representative of the individual cells in the multi-cell stack, were fabricated from reduced tubes approximately 6 cm long x 0.96 cm O.D. Electrode length was 5–5.5 cm except in the case of cells used in high-current density experiments, where shorter electrode lengths of 0.89–1.15 cm were used.

The cells were sealed to an alumina riser approximately 30 cm long x 1.27 cm Ø with a 0.64 cm bore using a CaO-MgO-Al_2O_3-SiO_2 (CMAS) based glass-ceramic sealant. Use of a riser allowed the entire length of the cell to be located in the uniform hot zone of a furnace during testing. The other end of the cell was sealed to a 1.3 cm diameter x 1.5 cm long cap of interconnect material (Ni, Cu or Ag/glass-ceramic composite) using the same CMAS glass-ceramic sealant. The interconnect cap had a recess at one end (1 cm diameter x 0.3 cm deep) which housed the end of the tube and a conductive washer of partially heat-treated metal/glass composite material, simulating the arrangement used multi-segment stack sealing. Sealing was carried out at a temperature 950–1000°C in an Ar/5% H_2 atmosphere using a small axial load (1–2N) to ensure that good contact was maintained between joint surfaces and sealant material and between the end of the tube, the conductive washer and the interconnect cap during the sealing cycle. Finally, a current collector consisting of porous Ni ink, hand brushed onto the surface of the outer electrode, and an overlying nickel mesh was applied and subsequently fired at 950°C.

PCER stack setup

The multi-segmented cell stack was produced by sealing repeating units of six membrane segments. The membrane segments were produced as described above, with an

active electrode length of 5.5 cm. The repeating element consisted of the six membrane segments sealed to the upper surface of a 3.9 cm diameter interconnect plate using a CMAS glass-ceramic sealing material.

Six recesses were machined on both the upper and lower surfaces of the interconnect plate to locate the ends of the membrane tubes. Conductive washers (sintered, but not crystallized Ni/glass composite material) were placed in the upper surface recesses to ensure good electrical contact between the end of the membrane segment and the interconnect plate after sealing. The conductive washer material was converted to a Ni/glass-ceramic during the sealing cycle, providing an expansion-matched conductive bridge between the components. The sealing material was applied in the form of a 4 mm thick, sintered CMAS glass preform. Graphite jigs/dies were used to press the sealing material into place and to maintain alignment between the components during the sealing process, which was carried out at 950–1000°C in an 5% H_2 (bal. Ar) atmosphere with an axial load of 14 N. For the lowest element, the interconnect was modified to connect all gas channels into a common annular chamber.

These repeating units (including bottom manifold) were then stacked together with a top manifold and sealed using a CMAS glass-ceramic sealant. The sealant was applied as a sintered annular preform of CMAS glass, 1 cm in diameter, placed between the free end of the membrane tubes and lower surface of the interconnect in the element above. Sealing was carried out by first placing the stack inside a hollow graphite cylinder with a bore of 4 cm to ensure alignment of the components and then heated to 950–1000°C with an applied uniaxial load of 15 N. The seal design allows the sealant to both provide hermeticity and prevention of undesired electrical contacts.

The top manifold is fabricated in zirconia-toughened alumina (CoorsTek Inc.). The manifold has internal channels which distribute the incoming gas flow to three of the six gas channels in the stack, while combining the three corresponding exhaust streams. The diameter of the three exhaust channels was constricted (1 mm diameter orifice) within the top manifold to provide a more balanced flow between the individual streams. The top manifold consists of three profiled ZTA plates, stacked and bonded together with CMAS glass-ceramic sealant. The three layers were sealed together using a tape-cast sheet of the sealant, laser cut to match the sealing surfaces and avoid blocking the internal channels. The top ZTA plate has two profiled tubular stubs protruding from the top surface which act as connection points for gas inlet and outlet. Ferritic steel (EN 1.4762) connectors were sealed to the each of the stubs using a CMAS glass-ceramic sealing material. The co-axial geometry of the joint components within the seal area, with the steel on the outside, allowed a strong, hermetic, compressive-type seal to be realised.

Single cell reactor testing

The tubular reactor set-up consisted of the inner membrane tube and an outer Kanthal APMT (I.D. = 20.5 mm). The tubes were assembled onto a 316 SS Swagelok-based system providing electrical contacts and feedthroughs for thermocouples and gases. Two thermocouples were placed on the outer shell tube at the corresponding top and bottom of the membrane tube as well as one inside in the middle of the membrane tube. By utilizing these thermocouples, the heating zones of the reactor furnace were adjusted to an axial temperature difference of less than 10°C. A Ni tube (O.D. = 4.8 mm) served as the gas feed and current collector for the reaction side. To ensure contact between the membrane and Ni tube, Ni wool (American Elements) was inserted in the tube isolated from the interconnect with quartz wool, allowing for measurements of voltage drop across the interconnect cap. For outer current collection, Ag or Cu wire (0.25 mm), depending on the reaction studied, was braided around the interconnect and to the Cu or Ag rod connected to a custom-made current

feedthrough. Additional voltage probes were added in the top and bottom of the membrane tube as well as the interconnect, these were achieved with Ag or Cu wiring and insulated using Al_2O_3 tubes from the outside reactor and other contact point to the current collection wires in order to provide unbiased measurements. The temperature was controlled by a three-zone reactor furnace integrated to membrane reactor testing rig, see fig. S25 for process flow diagram (AP Miniplant). During the experiments, current was provided by a HAMEG HMP4040 instrument and voltage was measured at different points using a multimeter (Amprobe). The effluents from the feed and sweep sides of the reactor were analyzed by an Agilent 7890A gas chromatograph equipped with two Molsieve and one HP Plot Q columns as well as one TCD and one FID for analysis of the feed side and another TCD for analysis of the sweep side. For hydrocarbon operation, methane conversion, products selectivity and yields of CO and CO_2 were calculated on carbon basis. Coke formation was not observed in any of the experiments and has therefore not been considered. For NH_3 operation conversion was calculated both by closing the hydrogen and nitrogen balance. Hydrogen recovery, HR, was calculated for methane, biogas and ammonia operation on the basis of the measured hydrogen flows F_{H_2} of both outlets as

$$HR = \frac{F^{II}_{H_2}}{F^{I}_{H_2} + F^{II}_{H_2}}$$

where I and II denote the outlets of the reforming/cracking and hydrogen side, respectively.

NH_3 decomposition was evaluated in the aforementioned setup. NH_3 was fed from a pressurized stainless steel NH_3 tank (>20 bar) and a digital Coriolis mass flowmeter (Bronkhorst). The total pressure of the NH_3 decomposition experiments, both for anhydrous and aqueous feed, was 10 bara while the temperature was set to 750°C. In the case of anhydrous ammonia, the feed consisted of 13 mL/min NH_3 and 5 mL/min H_2O resulting in a pNH_3 of 7.25 bar and pH_2O of 2.75 bar. In the aqueous NH_3 case (35% NH_3 in H_2O) the feed consisted of 25 mg/min NH_3, 45 mg/min H_2O and 15 mL/min He, corresponding to pNH_3 of 3 bar.

Single tube biogas steam methane reforming was also evaluated in the aforementioned setup. A mixture of 16.6 mL/min CO_2, 19.50 mL/min CH_4, 12.7 mL/min H_2 and 42.7 mg/min H_2O was fed to the inside chamber, corresponding to a CO_2 content of 40%. The outer chamber was fed with 101 mL/min N_2 and 40 mg/min H_2O. The total pressure of the biogas experiment was 10 bar, and temperature of operation was 750°C.

For each experiment, mass balances were calculated to verify that the applied analytical procedures were consistent. The carbon balance from experiments using hydrocarbons as feed were calculated according to the following equations:

$$\text{Carbon balance} = \frac{F_{CH_4,\text{feed outlet}} + F_{CO_2,\text{feed outlet}} + F_{CO,\text{feed outlet}}}{F_{CH_4,\text{feed inlet}}}$$

For the experiments presented here, we obtained a carbon balance ≥ 100 %, suggesting no formation of coke. The hydrogen balance was calculated according to

$$\text{Hydrogen balance} = \frac{2 \cdot F_{CH_4,\text{feed outlet}} + F_{H_2,\text{outlet sweep}} + F_{H_2,\text{outlefeed}}}{2 \cdot F_{CH_4,\text{feed inlet}} + F_{CO,\text{outlet feed}} + 2 \cdot F_{CO_2,\text{outletfeed}}}$$

Here we have used the outlet flows of CO and CO_2 to calculate the utilized flows of steam as direct quantification of the outlet flow of water has larger uncertainties associated to it. For experiments using ammonia as feed the hydrogen balance is calculated using the following formula:

$$\text{Mass balance}\left(H_2\right) = \frac{3/2 \cdot F_{NH_3,\text{feed outlet}} + F_{H_2,\text{feed outlet}} + F_{H_2,\text{sweep outlet}}}{3/2 \cdot F_{NH_3,\text{feed inlet}}}$$

and for nitrogen:

$$\text{Mass balance}\left(N\right) = \frac{2 \cdot F_{NH_3,\text{feed outlet}} + F_{N_2,\text{feed outlet}}}{2 \cdot F_{NH_3,\text{feed inlet}}}$$

In experiments where a leakage through the membrane was observed, the mass balance calculations was extended to include any leaked gas species.

High-current experiments were run in the aforementioned setup. The inner chamber was fed with a mixture of 116 mL/min CH_4, 241 mg/min H_2O, 72 mL/min H_2, 6 mL/min He, while the outer chamber was fed with 82 mL/min N_2 and 20 mg/min H_2O. The total pressure for the high-current experiments was 5 bar. Experiments were run at 710–750°C, controlled by the inner thermocouple. Larger axial temperature differences (up to 35°C) were observed due to the high currents applied resulting in ohmic heating of the membrane. Interconnect + washer resistances of 8.0 and 7.1 mΩ were measured for Ni-GC and Cu-GC, respectively.

Voltage-compression ratio measurements (Fig. 1C) were performed using the aforementioned setup. The measurements were conducted at a total pressure of 10, 19 and 35 bars, with a small overpressure of up to 0.3 bar in the direction opposing the hydrogen partial pressure gradient to achieve the lowest dilutions. For all compression ratios, hydrogen was electrochemically pumped from the inside chamber to the outside chamber by passing a constant DC current of 50 mA/cm² while monitoring the total cell voltage, as well as the voltage drop across the interconnect + wires. For compression ratio < 1, the inner chamber was fed with 100 mL/min H_2 while varying the H_2 concentration of the feed/sweep inlet streams by dilution with N_2 or He to simulate a specific compression factor. The total flow of the outer chamber was furthermore varied in order to ensure low dilution during electrochemical pumping. Both chambers were fed with a constant H_2O concentration of 20 mg/min at 10 and 19 bar, and 15 mg/min at 35 bar. For compression factors >1 the gas flows to the chambers were swapped. The reported compression ratios are calculated from the average hydrogen partial pressures along the membrane during pumping as measured by GC.

High-pressure experiments

High-pressure tests were carried out using a high-pressure proof HT800-alloy tubular reactor, and a tubular oven exhibiting 5 cm isothermal region. The tubular electrochemical cell with ZTA cap was sealed to a support collar (ZTA) mounted on an Inconel 625 riser. The rest of the testing rig is made of 316 SS Swagelok fittings and valves. Electrical contacts (two pairs of gold lead wires) were inserted in the high-pressure chamber by using two insulated feedthroughs. Temperature was monitored with a thermocouple placed inside the reactor, near the cap of the tube, inserted using a 316 SS thermowell. For the inner current collection,

Ni wool (American Elements) was inserted at the end of the tube and braided to two isolated gold wires (diameter = 0.5mm) that allowed the connection point outside the reactor.

The gas flows were controlled by high-pressure (up to 300 bar) mass flow controllers; N_2 (50 mL/min) and H_2 (250 mL/min) for the inner part, and N_2 (500 mL/min) and H_2 (500 mL/min) for the outer part of the membrane. Two high-pressure adjustable back pressure regulators (BPRs) maintained the desired pressure upstream in both chambers. Water is introduced in the system by using two HPLC (Gilson) pumps and then evaporated and overheated electrically. The exiting gas streams were passed through water condensers equipped with recirculating liquid cooler. To avoid steam condensation in the set-up, all gas lines, valves, and BPRs were heat-traced using heating tapes. The gas streams were analysed using a Gas Chromatograph Shimazu GC-2030 endowed with Carboxen-1010 and TR-624 columns together with BID and FID detectors. High-pressure gas cylinders were utilized throughout the duration of the experiments. The feed gas consisted of pure H_2 mixed with variable water contents. The test operating conditions were set at 750°C, and pressures ranging from 100–150 bar with no pressure difference. To ensure <1 bar pressure difference between chambers, the system was pressurized at a 15 bar/h rate. For compression/decompression experiments, pH_2 gradients across the membrane were achieved by mixing a calibrated diluted hydrogen mixture (5% H_2 bal. N_2) gas cylinder with pure H_2, 100 mL/min of pure H_2 were fed in the inner chamber, and 5% water was also added in both gas streams. Moreover, the outer chamber outlet stream was diluted with Ar (25 mL/min) to act as standard for the gas chromatography analyses. The H_2 flow in the inner chamber was simultaneously recorded using a H_2 mass flow reader. Current-voltage measurements were conducted using an AMETEK potentiostat/galvanostat model VersaStat3-450.

PCER stack testing

The stack was assembled into a steel reactor shell consisting of a reactor tube (EN 1.4959, O.D. = 48.3 mm, wall thickness = 3.68 mm), top and bottom lid. Mineral insulated cables with a steel outer sheath and copper as conductor was employed as electric feedthroughs, whereas copper rods/wires served as internal conductors from the ceramic stack to the feedthroughs. Steel tubing penetrating the top lid connected to the top gas manifold brought gas in an out of the ceramic stack. The sweep inlet was on the bottom lid while the produced hydrogen exited the top lid. The lids and reactor tube were finally joined by orbital gas tungsten arc welding.

A process flow diagram of the test rig used for PCER stack testing is shown in fig. S26. Pressurized gas and liquid flows were supplied by mass flow controllers (Bronkhorst) and mixed at room temperature. Steam was then generated using electrically heated tubular evaporators and brought to both sides of the stack. The feed gas consisted of a mixture of 23.5% CH_4, 60.8% H_2O, 14.5% H_2 and 1.2% He, resembling a gas composition from a pre-reformer (except CO and CO_2), operating at around 500 °C and with an initial steam-to-carbon ratio of 2.5. He was used as an internal standard. For the biogas experiments, the feed gas consisted of a mixture of 20.3% CH_4, 13.6% CO_2, 52.5% H_2O, 12.6% H_2 and 1.1% He, corresponding to a methane to CO_2 content of 60:40. The inlet sweep gas was a mixture of 45% N_2 and 55% H_2O.

Electric power to the stack was applied in galvanostatic mode employing an EA-PS 9040-120 DC power supply allowing up to 120 A. Five thermocouples were placed on the outside of the reactor shell, and upon changes in the current applied to the stack, the temperature was adjusted by means of a vertical split furnace with three individual heating zones to within ±10°C of the temperature studied, utilizing these thermocouples. Downstream of the stack, the gas streams pass through water-chilled condensers before liquid water is

stripped off in a gas-liquid separator. The remaining gas streams then pass volumetric flow meters (drum-type gas meter) to determine the total flow rate of the tail gas and hydrogen gas streams. The pressures of both stack chambers were controlled by dome-loaded pressure regulators (Equilibar) placed after the gas-liquid separator.

A known flow rate of both product gas streams was routed to a gas chromatograph (Agilent 990 Micro GC) to simultaneously determine the gas compositions of both product streams. He, H_2, N_2, CH_4, CO were detected through a Molsieve 5 A (MS5A) column where Ar was used as carrier gas, whereas CO_2 was detected by means of a PoraPLOT U (PPU) column where He was used as carrier gas. The GC was equipped with a thermal conductivity detector (TCD).

Methane conversion, products selectivity and yields of CO and CO_2 were calculated on carbon basis. Coke formation was not observed in any of the experiments, and also not expected from thermodynamic considerations, and has therefore not been considered. Hydrogen recovery, HR, was calculated on basis of the measured hydrogen flows F_{H_2} of both outlets as

$$ \mathrm{HR} = \frac{F_{H_2}^{II}}{F_{H_2}^{I} + F_{H_2}^{II}} $$

where I and II denote the outlets of the reforming and hydrogen side, respectively.

For each experiment, mass balances were calculated to verify that the applied analytical procedures were consistent. The carbon balance from experiments using hydrocarbons as feed were calculated according to the following equation:

$$ \mathrm{Carbon\ balance} = \frac{F_{CH_4,\text{feed outlet}} + F_{CO_2,\text{feed outlet}} + F_{CO,\text{feed outlet}}}{F_{CH_4,\text{feed inlet}}} $$

The inlet methane flow was determined in separate experiments using a high precision film flow meter (Horiba Stec). For the experiments presented here, we obtained a carbon balance ≥ 100 %, suggesting no formation of coke. The hydrogen balance was calculated according to

$$ \mathrm{Hydrogen\ balance} = \frac{2 \cdot F_{CH_4,\text{feed outlet}} + F_{H_2,\text{outlet sweep}} + F_{H_2,\text{outlefeed}}}{2 \cdot F_{CH_4,\text{feed inlet}} + F_{CO,\text{outlet feed}} + 2 \cdot F_{CO_2,\text{outletfeed}}} $$

We here use the outlet flows of CO and CO_2 to calculate the utilized flow of steam in the process as a direct quantification of the outlet flow of water has larger uncertainties associated to it. In experiments where a leakage through the stack was observed, the mass balance calculations was extended to include leaked gas species.

Multiphysics modeling and simulations

A multiphysics model of the PCER for production of hydrogen from methane, biogas and ammonia was developed for simulation of thermo-fluid-dynamics with current distribution. Coupled partial differential equations (PDEs) are used to model the physics in a 3D geometry, which are solved with the finite element method (FEM) in the COMSOL Multiphysics software. The conservation laws for momentum, mass, energy, and charge are represented, giving the fields for gas flow velocities and pressure, chemical species mass fractions, temperatures, and electric potentials in the stack. The complete set of equations are given in table S3. The nonlinear equation set is solved with damped Newton iterations in a

fully coupled solver, and the direct PARDISO method is used for solving the linear systems. All solutions are obtained when the relative error is below a tolerance of 10^{-3}.

Fluid flows

The gas flows are modeled with the compressible laminar Navier-Stokes equations, with the Brinkman equation for the porous domains (Ni cermet support). Material specific properties are given in table S4. The ideal gas law is used for calculating fluid density, and mixture dynamic viscosity is computed with the Wilke model (*19*). The inlet mass flow rates are specified at the reforming/decomposition side and sweep side inlets, respectively, and the pressure is fixed at the outlets.

Mass transport

The mass fractions of the species on the reforming/decomposition side (CH_4; CO; CO_2; H_2; H_2O/NH_3; N_2; H_2; H_2O) and on the sweep side (H_2; H_2O) of the membrane are solved for with a mixture averaged model for diffusion and convection. Mass sources are introduced in the catalytic porous supports, coupled to the chemical reaction rate expressions. At the membrane boundary, the H_2 flux is coupled with the membrane current density. Temperature dependent species properties are used, and binary diffusion coefficients are computed with the Fuller-Schettler-Giddings model (*20*). The thermophysical properties of the species are obtained from the built-in thermodynamic property package in COMSOL Multiphysics. Inlet species molar fractions are specified at the reforming/decomposition side and sweep side inlets, and mass flux at the outlets are constrained to convection-only (zero diffusive flux).

Chemical reaction kinetics

The kinetics of the steam methane reforming, water-gas shift, and the overall reaction ($CH_4 + 2H_2O \leftrightarrow 4H_2 + CO_2$) reactions are modeled adopting a kinetic model and adsorption equilibrium constants from Xu & Froment (*21*) with experimentally fitted rate coefficients (fig. S28). The rate equations are limited by the thermodynamic equilibrium, coupled with the local partial pressures of the species on the reforming/decomposition side and temperature. When fed with biogas, the kinetics of the dry reforming reaction ($CH_4 + CO_2 \leftrightarrow 2H_2 + 2CO$) is also introduced. For ammonia decomposition (ES1) the kinetics are based on the (equilibrium limited) Temkin-Pyzhev rate equation (ES2) with addition of a rate inhibition effect of steam (ES3). Assuming the resulting rate equation with steam inhibition (ES4) in a continuous reactor model (plug flow reactor), the kinetic coefficients were adjusted to fit the measured conversions from fixed-bed reactor experiments performed at high NH_3 partial pressure and high temperature. More details are given in table S3 and the fitted kinetic parameter values in table S5.

$$2NH_3 \leftrightarrow N_2 + 3H_2$$

$$r_{A1}^0 = k_{A1} \left(\frac{p_{NH_3}^2}{p_{H_2}^3} \right)^{\beta_{A1}} \cdot \left[1 - \frac{p_{N_2} p_{H_2}^3}{K_{eq,A1} p_{NH_3}^2} \right]$$

$$\lambda_{A1} = \left(1 + K_s p_{H_2O} \right)^{-\alpha_{A1}}$$

$$r_{A1} = r_{A1}^0 \lambda_{A1}$$

Electric potentials

The electric potentials are modeled with Ohm's law with charge conservation in 3D in the inner electrodes (anodes) and interconnects, and in 2D in the thin outer electrodes (cathodes) and current collectors. The electrical conductivity of the electrode and

interconnect materials were obtained from measurements of these components and modeled with a temperature dependency equal to nickel material (*22*). The potential difference between the anode and cathode across the electrolyte is decomposed into a reversible and an irreversible term, given by the local Nernst potential and the product of the local current density and the area specific resistance (ASR) of the membrane-electrode assembly, respectively. The local normal current density across the membrane-electrode assembly is solved for by applying Ohm's law. The applied current is specified at the outer electrode surfaces of the six topmost parallel cells of the reactor, while the bottom interconnect is set to zero electric potential (ground).

Heat transfer

Heat transfer is modeled with the heat balance equation, which accounts for heat transfer by convection and conduction in gases, porous domains, and solid materials. Volume-averaged effective thermal properties are used for the porous support. For gases, the mixture averaged heat capacity is used, while thermal conductivity is computed with the Wilke model. Volumetric heat sources from the chemical reactions are included in the porous supports, in addition to the Joule heat from ohmic power dissipation in the inner electrodes and interconnects. The electrochemical cells are modeled as 2D boundary heat sources, accounting for the resistive (ohmic) and reversible (electrochemical) contributions. Upstream temperatures of the inlet gas streams are specified. The outer boundaries of the reactor (the outside surface of the reactor shell) allow for heat exchange with a surrounding domain fixed at the operating temperature to emulate operation in a temperature-controlled environment. Internal heat exchange between cells is illustrated by heat flux from cells in fig. 27.

Comparison with experiments

Simulation results from the multiphysics model has been evaluated to a SEU experiment where a thermocouple was placed inside the SEU in the center of the first barrel. This enables to track temperature changes inside the SEU in addition to the thermocouples placed on the reactor shell. The comparison is shown in fig. S28.

System modelling of scalable fuel-flexible stacks

The heat and mass balances of hydrogen production systems operating on four different fuels (methane, biogas, anhydrous NH_3 and aqueous NH_3) and high-temperature steam electrolysis (HT-WEL) were modelled using Aspen Plus V10, and the corresponding process flow diagrams and major assumptions can be found in figs. S17, S18, S19, S20 and S21, respectively. The model for the fuels includes a simplification of the PCER using a sequential model, dividing the reactor axially into -n multi-sub-reactors and n-1 sub-separators. A first Gibbs reactor is followed by a series of selective hydrogen separators with constant extraction in each, and a Gibbs reactor to re-equilibrate all the reaction products upon hydrogen extraction. An excess of catalyst was assumed to guarantee that equilibrium is reached. The model of the HT-WEL reactor has been simplified in Aspen by a stoichiometric reactor based on known fractional conversions. In both cases the reactor model in Aspen is coupled with an external calculator for the electrochemical energy balance. In addition to the reactor model the processes include steam generation unit, heaters and heat exchangers system and condensation units.

System efficiency was calculated as

$$Efficiency(\%) = \frac{F_{H_2} \times HHV_{H_2}}{F_{fuel} \times HHV_{fuel} + W_{electric}} \cdot 100$$

where F_n is the flow rate of component n, HHV_n is higher heating value of component n, and $W_{electric}$ is the total electric power consumption. The following high heating values were used for each fuel: hydrogen 141783.3 kJ/kg, methane 55515.1 kJ/kg, biogas 19619.3 kJ/kg, liquid anhydrous ammonia 21084.3 kJ/kg (evaporation of the ammonia is part of the energy balance) and aqueous ammonia 22478.8 kJ/kg. These heating values enable to introduce the term of the "chemical energy" of the feed molecules in the overall mass balance. For the energy balance calculations, losses associated to transformation and rectification of the input alternating current is included, assumed to be 98% efficient. For all fuels, a heat loss to surroundings of 17 kW from the 1 ton/day generation units is assumed through the thermal insulation of membrane packs. Energy balances and system efficiencies calculated in the system models are presented in the form of Sankey energy diagrams in figs. S15 and S16. Assumptions are detailed in figs. S17 to S21.

Carbon emissions calculations and assumptions

The methodology for carbon emissions calculations of fig. S22 are described in fig. S23. It is based on well-to-wheel analysis for vehicle emissions, where all the emissions from the primary fuel used up to the driving of the vehicle are included. Primary fuel is defined as the raw materials used for production of the final fuel, called road fuel, defined as the fuel on which the vehicle will be driven.

For the PCERs and HT-WEL vehicles the road fuel is hydrogen, and the primary fuels are methane and electricity for the methane case, biogas and electricity for the biogas case, liquid ammonia and electricity for the dry and aqueous NH_3 cases. Column A: Own calculations, can be derived from Sankey in figs S15 and S16. Column C: Own calculations, from mass balance of the PFDs shown in figs. S17 to S21. Column E: Emissions related to liquefaction of CO_2 and CO_2 transportation.

ICE-diesel data point made bigger in fig. S22 for visibility.

Materials usage

Materials usage of the ceramic stack and the reactor shell includes estimation of scrap during the different production steps. Although it is expected that recycling of materials along several of the fabrication steps is feasible, it was assumed that this was not implemented, and the materials usage calculations is therefore higher than can be expected for a large fabrication plant. All elements below 0.6 wt.% in the stack were not included in materials usage unless a rare earth or low-availability material. MgO in the stack calculation is also including MgO in the reactor (high-temperature insulation of wire).

Microscopy

Scanning electron microscopy was conducted on a tube cross-section that had been mounted in epoxy and polished to a finish of 0.06 μm (colloidal silica). Backscatter electron micrographs were taken with a FEI Quanta 200 FEG-ESEM at 15 keV in low-vacuum mode (60 Pa) to reduce sample charging.

Kinetic measurements

Dedicated fixed-bed experiments were carried out in order to determine the SMR kinetic parameters and the fitting to the considered model. The elucidation of the kinetic parameters (k_{M1}, k_{M2} k_{M3}) considers the reactions involved in the PCER operation (see fig. S29A), according to the model proposed and the adsorption parameters by Xu and Froment (21). The combined effect of parameters such as temperature, pressure, residence time and feed composition were studied. The conditions were set to approach the different regimes

encountered along the PMR length. i.e. SMR inlet, SMR reaction shifting and water gas shift (WGS) reaction. The obtained results enabled to improve the accuracy and fidelity of the Multiphysics PCER model under a broad range of operating conditions. To improve the accuracy in the determination of WGS reaction kinetics, specific experiments were carried out. Finally, SMR reaction results were used along with the WGS reaction results to obtain the full set of kinetics parameter and the later model validation. The goodness of the resulting fitting can be observed in fig. S29B, where the experimental results are plotted with respect to the model predicted values. As it can be seen, the model is able to predict conversion and yield values with high confidence (deviation lower than 10%). Table S5 depicts the fitted kinetic parameters, including associated activation energy values. Statistically, the estimated kinetic parameters present a 95% confidence interval of $\pm 8\%$ for pre-exponential constants and $\pm 4\%$ for activation energy values. Pre-exponential constants are calculated in dependence of BET area.

An additional experimental kinetic study using biogas as feed was also considered. The objective was to adapt the kinetic model previously developed for the feeding and reaction conditions encountered in the biogas reforming. During these reforming tests, variables such as CH_4 conversion and CO and CO_2 selectivity were monitored during the reaction time. The kinetic results included the additional dry reforming reaction (B1: $CH_4 + CO_2 \leftrightarrow 2H_2 + 2CO$) that becomes important in the reaction network with biogas feed. An accurate fitting for specific operation with biogas is obtained, as illustrated in the parity plot (fig. S29C).

Stability under high hydrogen recoveries

In order to study the potential Ni oxidation of the internal PCER electrode, a series of tests considering a high degree of H_2 recovery (above 99%) were performed. The objective is to mimic the expected conditions through the last section of the PCER, where the high degree of H_2 recovery will lead to atmospheres with high H_2O and CO_2 concentration allowing us to evaluate the stability of the WGS catalytic performance. In addition, such chemical environments may potentially induce the oxidation of Ni particles in the PCER electrode via these reactions; $Ni + H_2O \rightarrow NiO + H_2$ and $Ni + CO_2 \rightarrow Ni + CO$. Such conditions were mimicked by considering different CO_2/H_2 mixtures at 800ºC at 7 bar. Three different test runs were performed to study the oxidation after the exposure to different H_2 extraction regimes: Oxidation 1 (H_2 extraction of 99.67%), Oxidation 2 (H_2 extraction of 99.81%), and Oxidation 3 (H_2 extraction of 99.88%). The Ni/BZCY material was as such, subjected to a series of consecutive steps with oxidizing (CO_2/H_2 mixture) and reducing (H_2 feeding) atmospheres (fig. S30). By monitoring the transient evolution of H_2 molar fraction upon switching from oxidizing to reducing conditions it is possible to identify the possible material oxidation. Fig. S30 displays the molar fraction evolution of H_2, CH_4, CO and CO_2 during the reduction-oxidation cycle tests. No signs of H_2 transient response—denoting a H_2 consumption by an oxidized species—is detected. Only a little variation in H_2 molar fraction evolution can be observed in the Oxidation 3 step transient. The transient in H_2 molar fraction in the reduction step could potentially be ascribed to the reduction of NiO species formed in the preceding oxidation step. Nevertheless, the fast reduction kinetics and the GC measurement timescale (2 min) only enables the qualitative diagnosis of the process. From the XRD and temperature-programmed reduction (TPR) measurements on samples after cyclic oxidation tests, it was possible to determine the amount of Ni oxidized to NiO during the oxidation treatments. The sample subjected to Oxidation 3 conditions exhibits the highest oxidation degree, with ~12% of oxidized Ni as for XRD and TPR measurements. These results were confirmed by SEM and EDX analyses. High H_2 recovery above 99.88% may

lead to Ni oxidation into NiO at 800ºC, however, it is fully recovered and functional when followed by a reduction (regeneration) step.
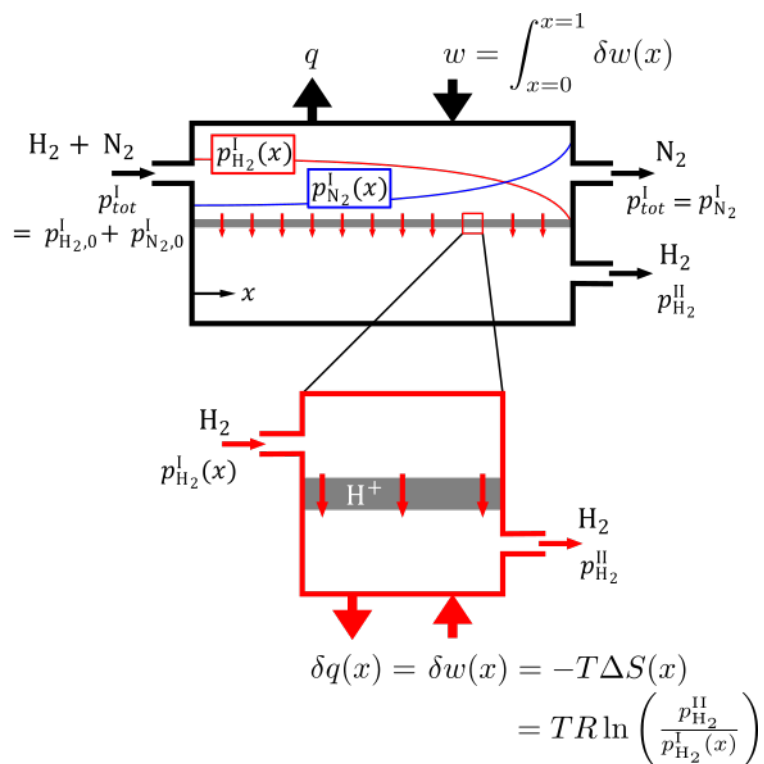
Fig. S1. Continuous compression and separation process.

The continuous flow process with compression and separation of H_2 from a mixture of N_2 and H_2. In the global system (black) the extent of separation, and thus partial pressure of H_2 (and N_2), varies with the reactor coordinate x. The localized system (red) considers isothermal compression of H_2 from the local partial pressure on side *I* of the membrane to a constant partial pressure on side *II*. The locally isothermal process produces an amount of heat equal to the compression work, which must be either expelled external to the global system (resulting in a globally isothermal process) or absorbed by the global system. If the absorbed heat causes a change in temperature of the global system, the overall process becomes non-isothermal. Detailed equations found in table S6.
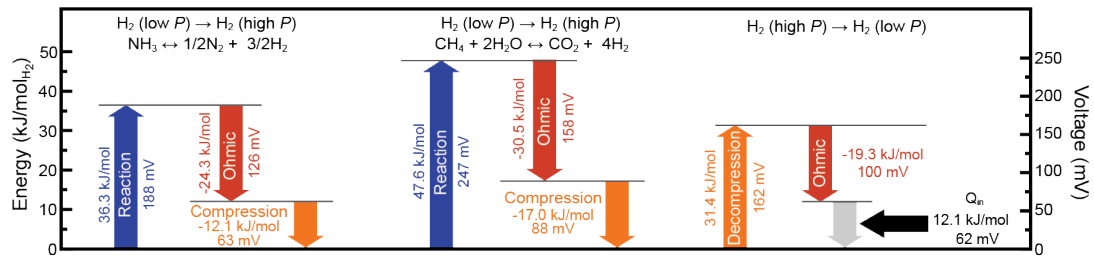
Fig. S2. Combining reaction and separation for hydrogen from NH₃, CH₄, and biogas.
Energy balance and correlated voltages for three different thermoneutral operating modes which include reaction ($E_R=\Delta H_R$ and $U_R=\Delta H_R/nF$), charge transport ($E_C=iRnF$ and $U_C=iR$) and compression/decompression ($E_{co}=U_N nF$ and $U_N= RT/nF \ln(pH_2^{II}/pH_2^{I})$) for SMR+WGS at 750°C with a H₂ compression ratio 7.4, NH₃ cracking at 650°C with a H₂ compression ratio 5.4 and a hydrogen concentration cell at 750°C with a H₂ compression ratio of 0.025. Q_{in} for the H₂ concentration cell is the heat required from the surroundings to achieve thermoneutral operation.
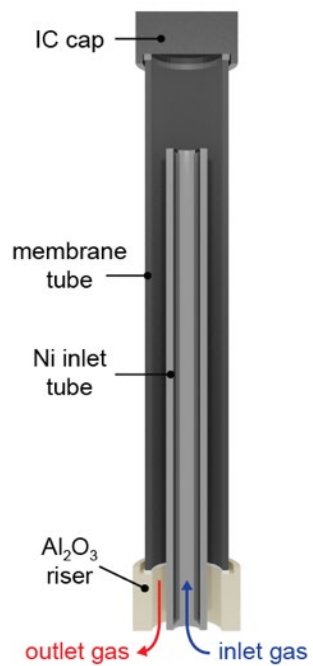
Fig. S3. Representative single cell schematic.

Representative single cell sample consisting of the core elements: tubular electrochemical cell, IC cap, and IC washer (between cap and membrane tube) used for single cell testing.
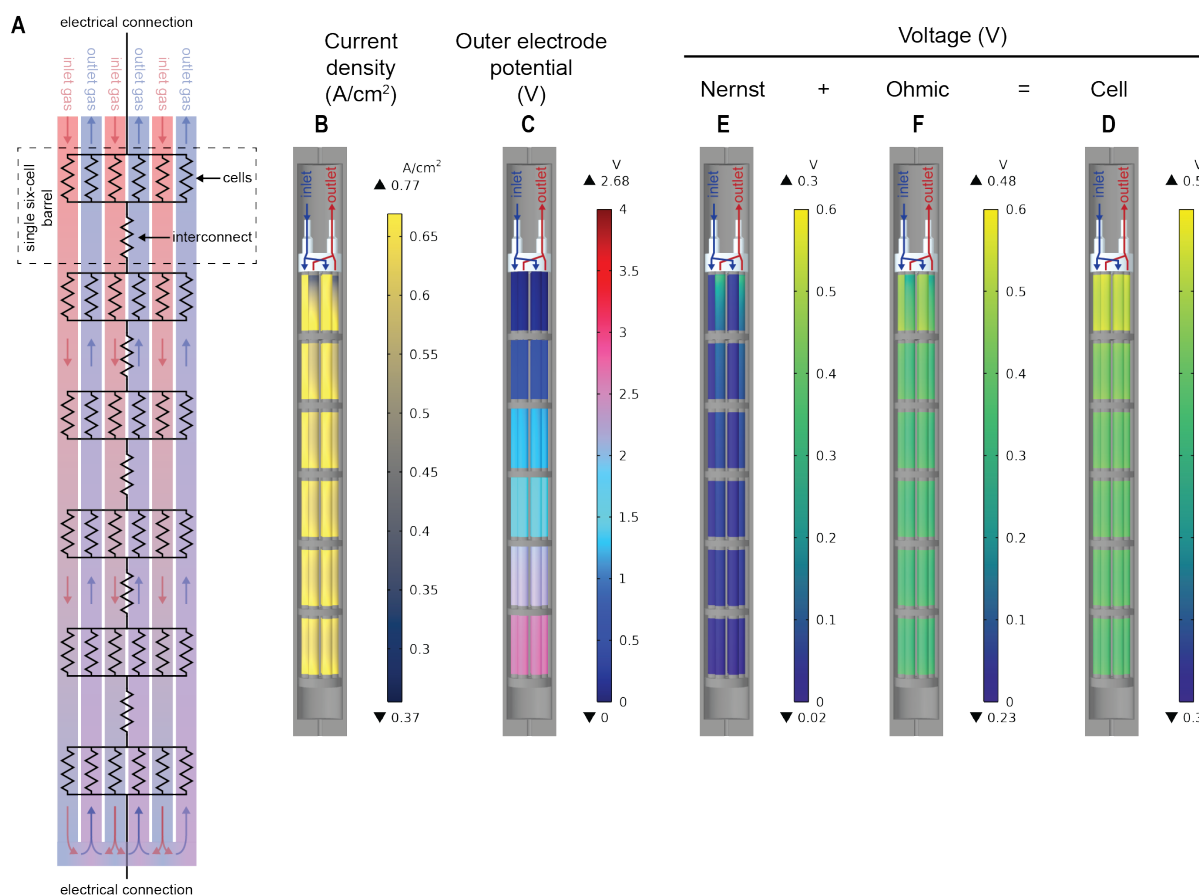
Fig. S4. PCER stack electrical circuit with multiphysics simulations.

(**A**) Schematic of the electric circuit and flow directions in a 36 cell multi-segmented reactor, consisting of 6 barrels in series with 6 parallel proton ceramic cells in each. (**B-F**) Output from multiphysics simulations, illustrating the steady-state results for a reactor operating at 750°C, 20 bar total pressure on both sides of the membrane, mean current density of 0.61 A/cm^2, producing 0.30 kg/day separated H_2 with 99.09% hydrogen recovery, 99.99% methane conversion and 92.95% CO_2 yield. Feed: 28.57% CH_4 (0.597 NL/min), 71.43% H_2O. Sweep: H_2O (0.18 g/min). The simulations show that the current density varies between subsequent single cells, especially in the top barrel, where the inlet cells has a higher current density that the outlet cells. We see that it is the Nernst voltage that governs the current distribution because of the high compression ratio in the outlet cell. A higher current density is therefore observed in the inlet cell despite that these cells have a lower temperature, which leads to an increased cell resistance.
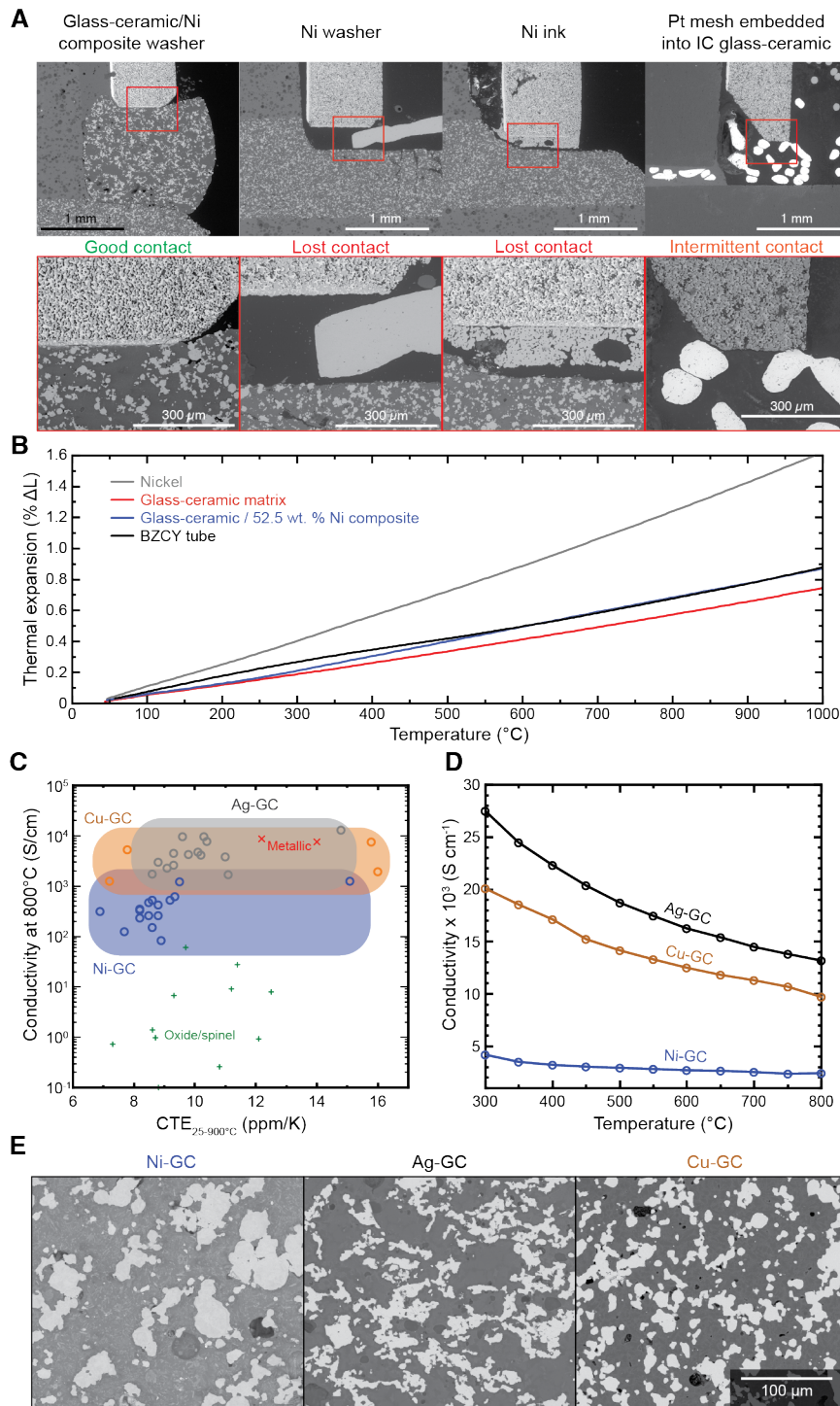
Fig. S5. PCER interconnect washer architecture comparison and additional materials properties.

(**A**) Comparison of different electrical connection types from the BZCY/Ni support to the interconnect after five thermal cycles from room temperature to 800°C in hydrogen at 5°C/min. The glass-ceramic/Ni composite washer (similar composition to that of the interconnect) maintained excellent electrical contact after the thermal cycles and exhibited chemical bonding of the nickel from the composite washer to the nickel in the BZCY support. The Ni washer lost electrical contact between the BZCY support and interconnect and exhibited a physical separation due to the difference in thermal expansion. Nickel ink

27

(painted on the interconnect before insertion of membrane tube) maintained good contact with a chemical bond to the support, however it separated from the interconnect due to the expansion mismatch and consolidation of the nickel ink after the binder burned out. A concept to integrate a Pt mesh as the conductive interconnect material where it also functions as a washer was also examined, and it demonstrated intermittent electrical contact, also due to thermal mismatch. (**B**) Linear thermal expansion (cooling curves) of nickel metal, the glass-ceramic matrix used in the IC, the glass-ceramic composite IC material, and the BZCY/Ni support as a function of temperature. Incorporating nickel into the glass-ceramic matrix increases the thermal expansion coefficient to bring the composite expansion up to a level which provides an excellent match to the BZCY/Ni support. However, the magnitude of the increase in CTE is much less than might be expected from a rule of mixtures, considering the CTE, elastic modulus and volume ratios of the two materials (*23*). This is considered to be a consequence of poor bonding between the nickel and glass-ceramic phases in the absence of an interfacial oxide layer, and possibly also due to some level of plastic deformation in the nickel as the composite cools after processing or service at elevated temperature. The effect is considered to be analogous to the influence of Ni on the thermal conductivity of Ni-glass composites where poor interfacial bonding hinders heat transfer and leads to lower than expected thermal conductivity (*24*). The limited influence of the nickel on increasing the composite CTE is highly beneficial in that the percolation limit can easily be exceeded without compromising the expansion match to the BZCY/Ni support. (**C**) Conductivity at 800°C versus CTE (25–900°C) for Ag-, Cu-, and Ni-containing glass-ceramic (GC) interconnects as part of the investigational search to optimize the IC for this study. Cu- and Ni-GCs were measured in 5% H_2 (bal. Ar) and the Ag-GC was measured in air. Tabulated literature values in table S1. The compositional flexibility of the glass-ceramic system enables ICs that span coefficient of thermal expansions and electrical conductivities in a wide pO_2 tolerance range ($10^{-20} < pO_2 < 10$ bar). (**D**) Interconnect conductivity as a function of temperature. (**E**) Scanning electron backscatter cross-sections of Ag-, Cu-, and Ni-containing glass-ceramic (GC) interconnects. Bright appearance is the metallic phase and dark appearance the GC phase.
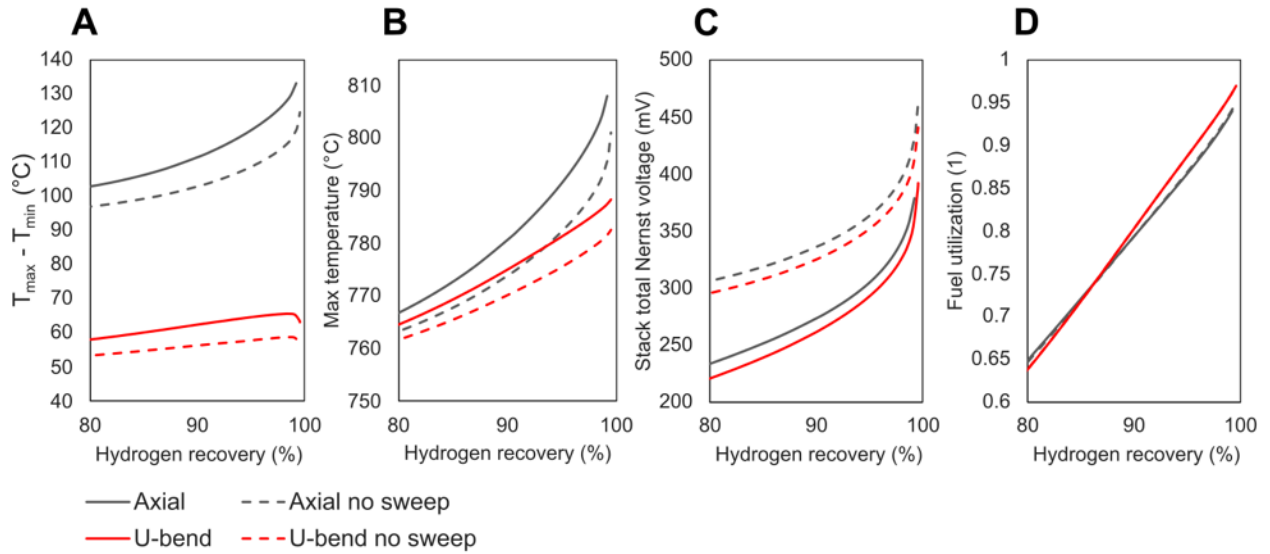
Fig. S6. Multiphysics simulation of axial and u-bend PCER varying hydrogen recovery.
Operating at 750°C with 20 bar total pressure on both sides of the membrane. Feed: 28.6% CH_4 (0.597 NL/min), 71.4% H_2O. Sweep case: H_2O (0.18 g/min). (**A**) Temperature difference in PCER. (**B**) Maximum temperature in PCER. (**C**) Total Nernst voltage of stack. (**D**) Fuel utilization (extracted fraction of hydrogen available in fuel). The resulting simulations shows that the temperature difference and maximum temperature is higher in the axial PCER compared to the u-bend PCER and that the difference increases with increasing hydrogen recovery. Operating without sweep gas lowers the temperature as transfer of excess heat from the membrane operation is improved by thermal conduction through pure H_2 vs a $H_2 + H_2O$ sweep mixture. The exponential feature of the axial PCER at high hydrogen recoveries is a result of the increased temperature as evident from the non-isothermal compression seen in Fig. 1B.

Fig. S7. Multiphysics simulation of multi-segmented PCER operation on methane.
(**A-G**) Output from multiphysics simulations, illustrating the steady-state results for a reactor operating at 750°C, 20 bar total pressure on both sides of the membrane, mean current density of 0.61 A/cm^2, producing 0.30 kg/day separated H_2 with 99.09% hydrogen recovery, 99.99% methane conversion and 92.95% CO_2 yield. Feed: 28.57% CH_4 (0.597 NL/min), 71.43% H_2O. Sweep: H_2O (0.18 g/min).

Fig. S8. Multiphysics simulation of multi-segmented PCER operation on biogas.
(A-G) Output from multiphysics simulations, illustrating the steady-state results for a reactor operating at 750°C, 20 bar total pressure on both sides of the membrane, mean current density of 0.61 A/cm^2, producing 0.30 kg/day separated H_2 with 99.05 % hydrogen recovery, 99.99% methane conversion and 92.29% CO_2. Feed: 24% CH_4 (0.597 NL/min), 16% CO_2, 60% H_2O. Sweep: H_2O (0.18 g/min).
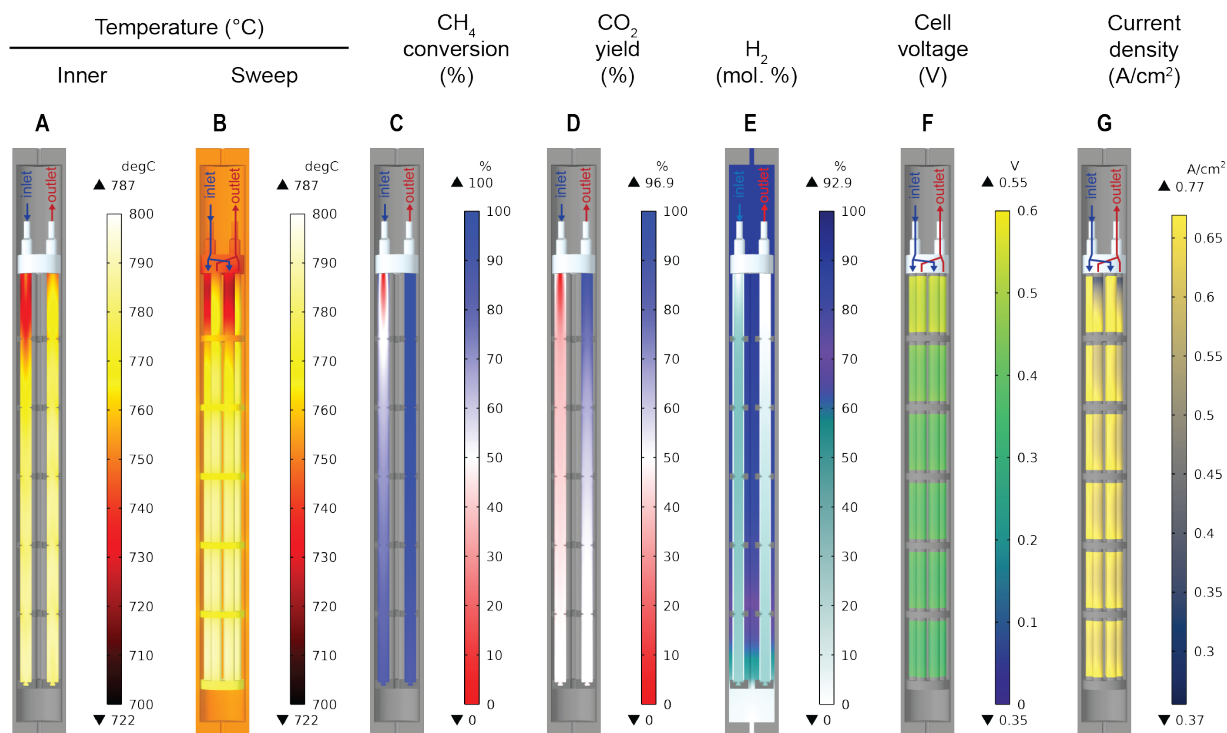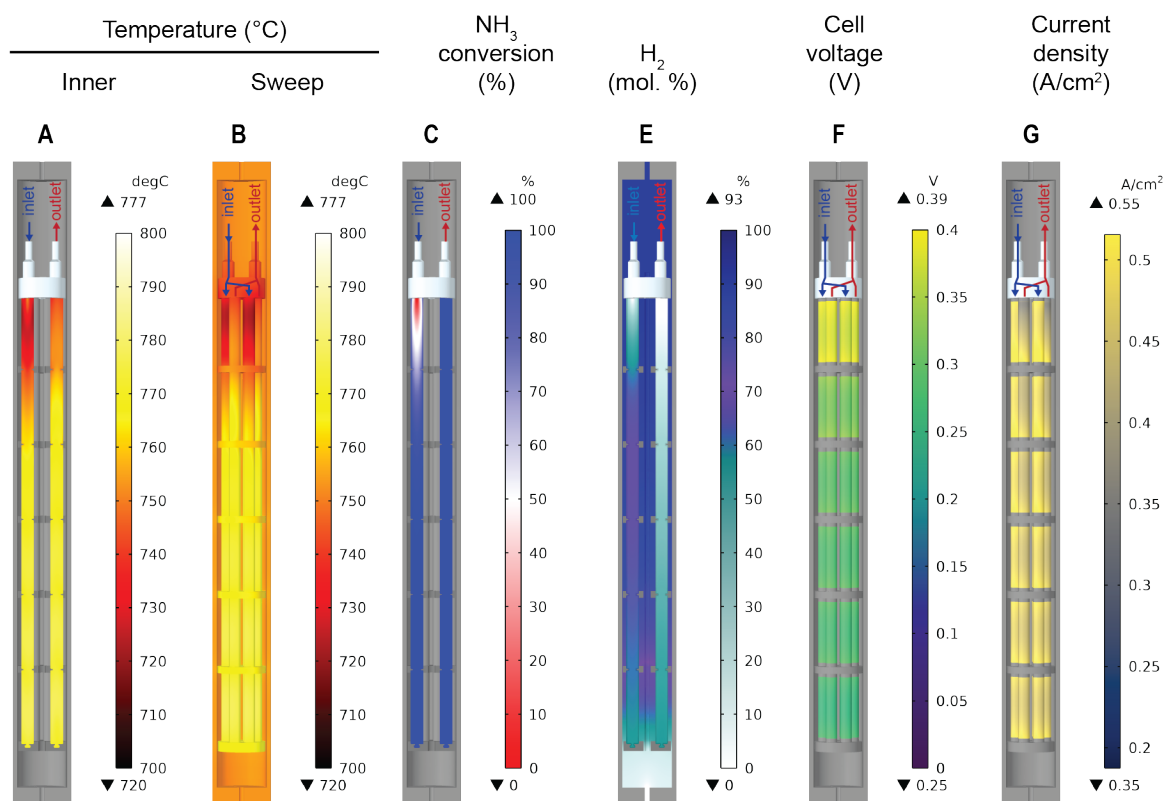
Fig. S9. Multiphysics simulation of multi-segmented PCER operation on anhydrous ammonia.

(A-F) Output from multiphysics simulations, illustrating the steady-state results for a reactor operating at 750°C, 20 bar total pressure on both sides of the membrane, mean current density of 0.45 A/cm^2, producing 0.22 kg/day separated H$_2$ with 98.27% hydrogen recovery, 99.99% ammonia conversion. Feed: 95.0% NH$_3$ (1.17 NL/min), 5.0% H$_2$O. Sweep: H$_2$O (0.13 g/min).
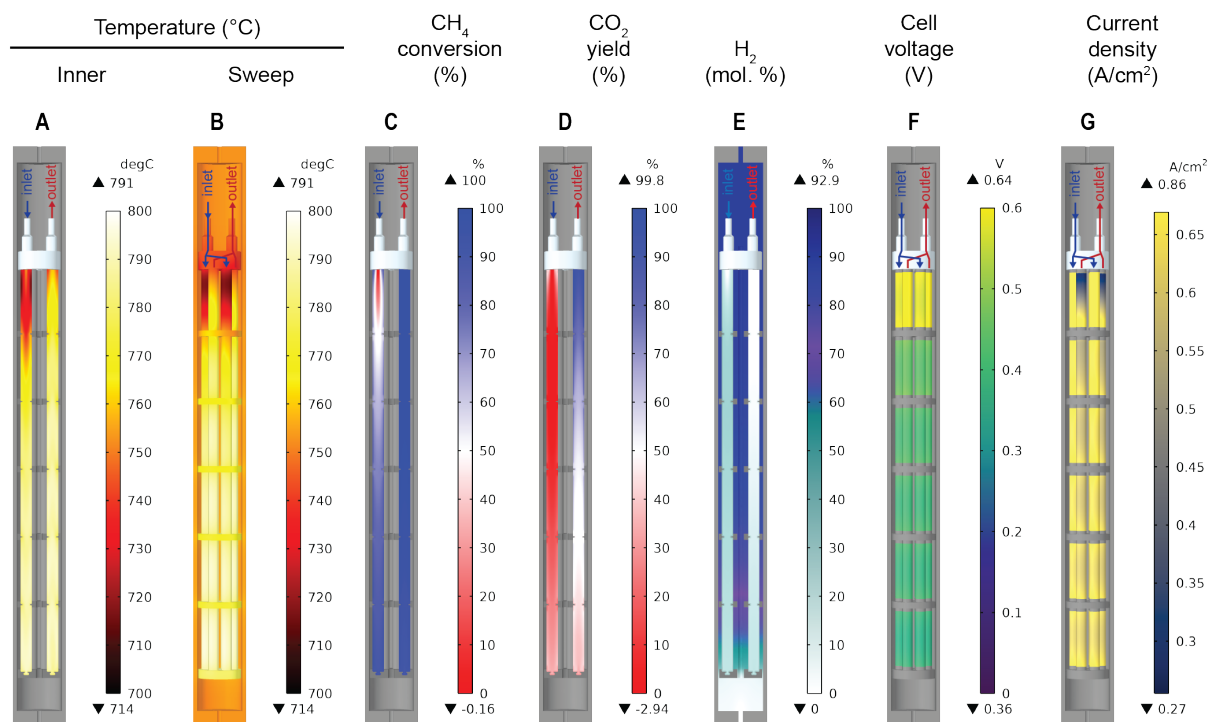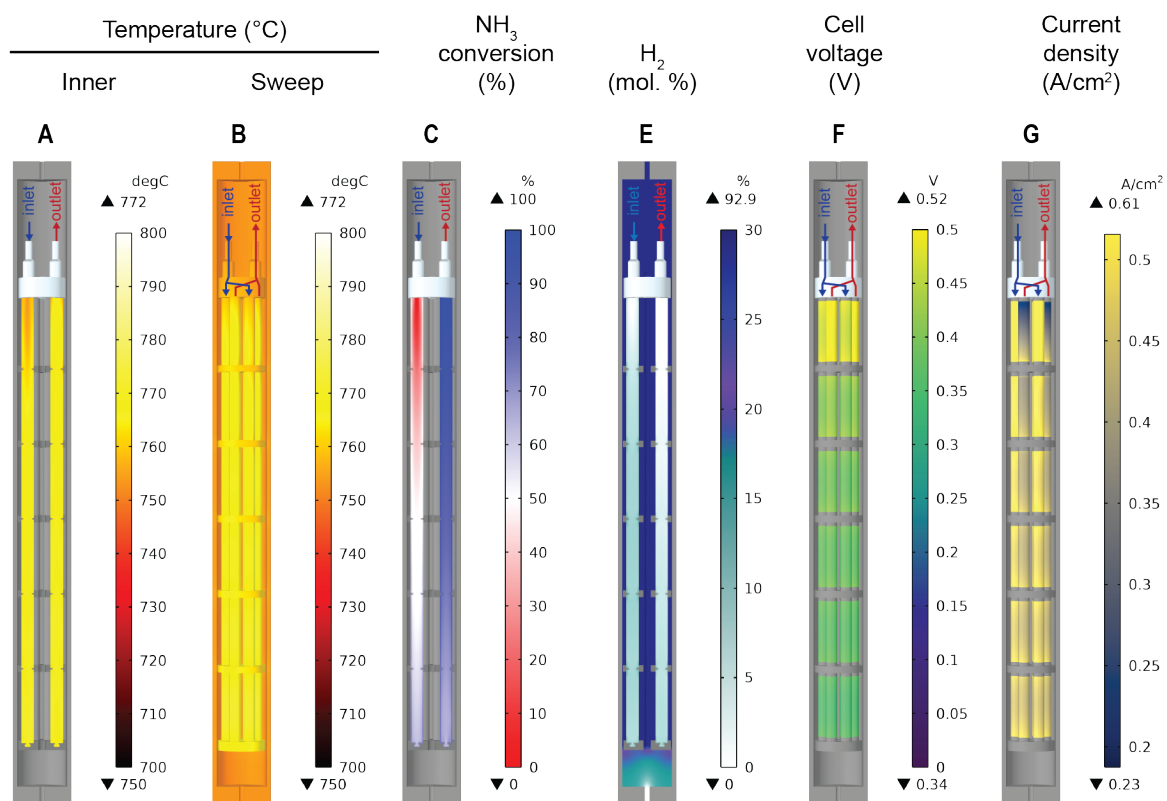
Fig. S10. Multiphysics simulation of multi-segmented PCER operation on aqueous ammonia.

(A-F) Output from multiphysics simulations, illustrating the steady-state results for a reactor operating at 750 °C, 10 bar total pressure on both sides of the membrane, mean current density of 0.45 A/cm^2, producing 0.22 kg/day separated H$_2$ with 98.31% hydrogen recovery, 97.67% ammonia conversion. Feed: 35.0% NH$_3$ (1.17 NL/min), 65.0% H$_2$O. Sweep: H$_2$O (0.13 g/min).
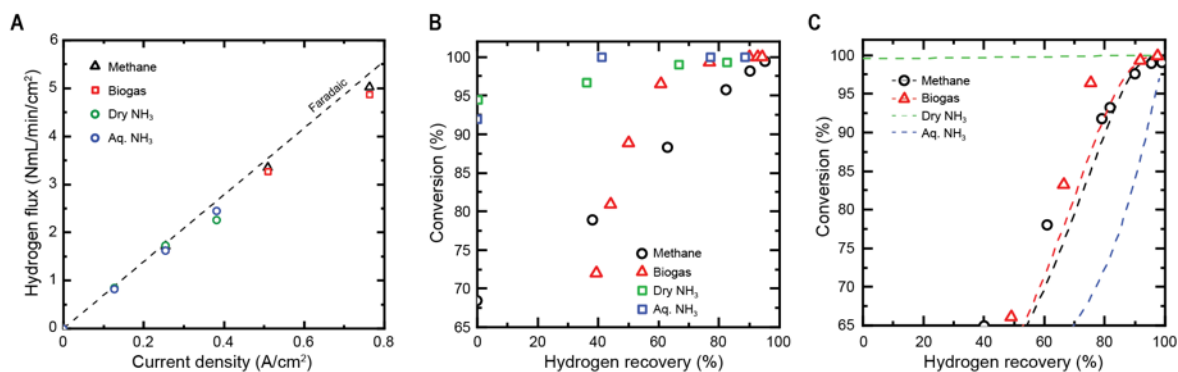
Fig. S11. PCER single cell and stack performance.
(**A**) Hydrogen flux versus current density for methane, biogas, anhydrous (dry) and aqueous ammonia at 750°C and 10 bar evaluated on a single cell. The dotted line is the faradaic pumping limit. (**B**) Single cell conversion as a function of hydrogen recovery for methane, biogas, anhydrous (dry) NH_3, and aqueous NH_3 ($H_2O/NH_3 = 1.85$) demonstrating close to 100 % conversion and 100 % hydrogen recovery. Single cell tests at 750°C, 10 bar. (**C**) PCER stack performance; conversion as a function of hydrogen recovery for methane, and biogas, compared with multiphysics model data (lines) for anhydrous NH_3, and aqueous NH_3. PCER stack tests and model at 750°C, 20 bar).
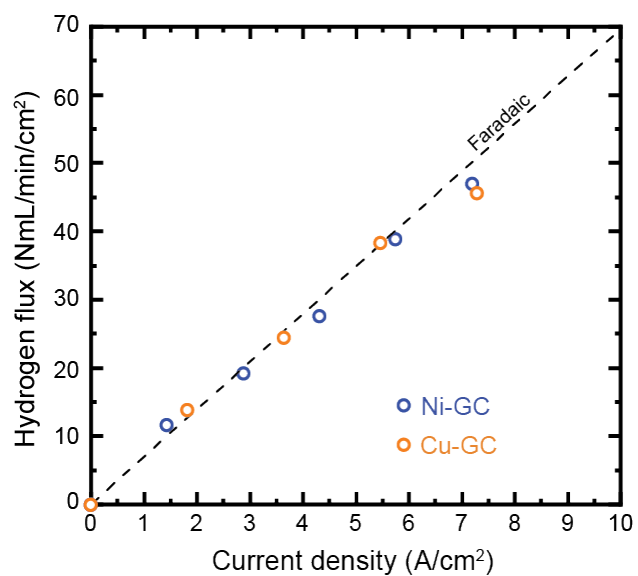
Fig. S12. Single cell performance at high-current.

Hydrogen flux versus current density in methane at 725–750°C, 5 bar, S/C=2.5 for representative single cell samples with both Ni- and Cu-GC interconnect materials. The dotted line is calculated faradaic flux.
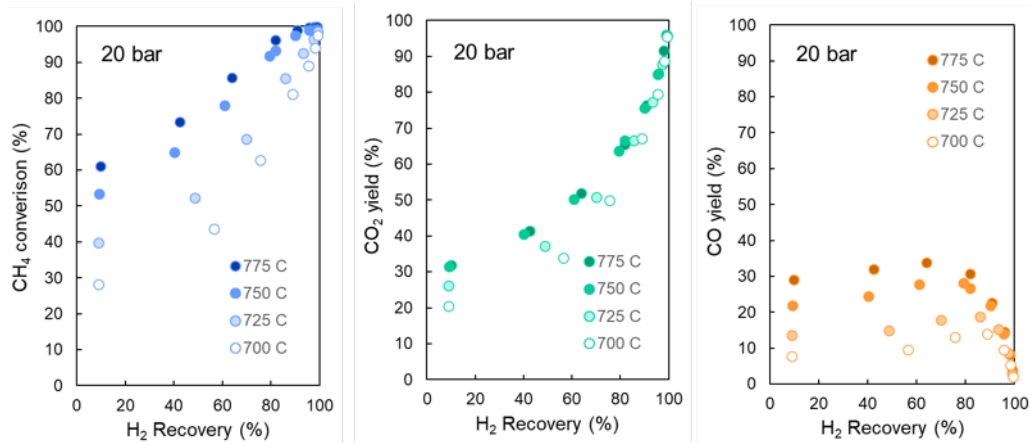
Fig. S13. Multi-segmented PCER stack performance with methane versus temperature.
Conversion, yield of CO_2, and yield of CO as a function of hydrogen recovery of multi-segmented stack of methane at 20 bar (S/C = 2.5) for the range of 700–775°C.
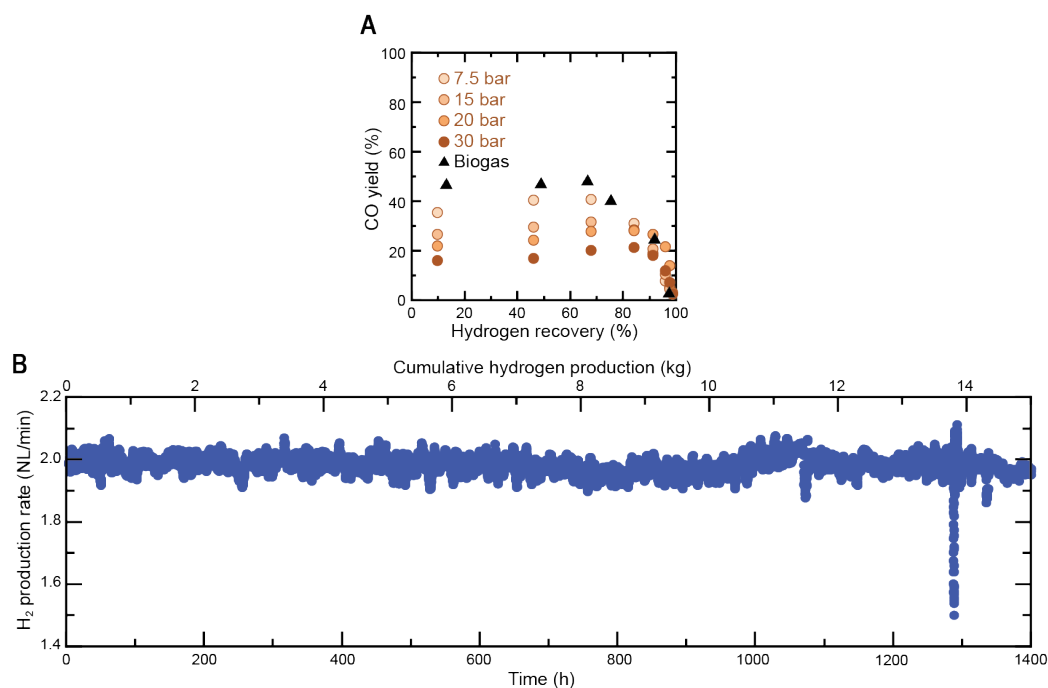
Fig. S14. Multi-segmented PCER stack performance and durability with methane and biogas.

(**A**) Yield of CO vs. hydrogen recovery of PCER stack at 750°C for the range of 7.5–30 bar methane and biogas at 20 bar. (**B**) H_2 production rate as a function of time (715–750°C, 5 bar, S/C = 2.5, FE = 96%). Cumulative hydrogen production (secondary x-axis) based on average production rate.
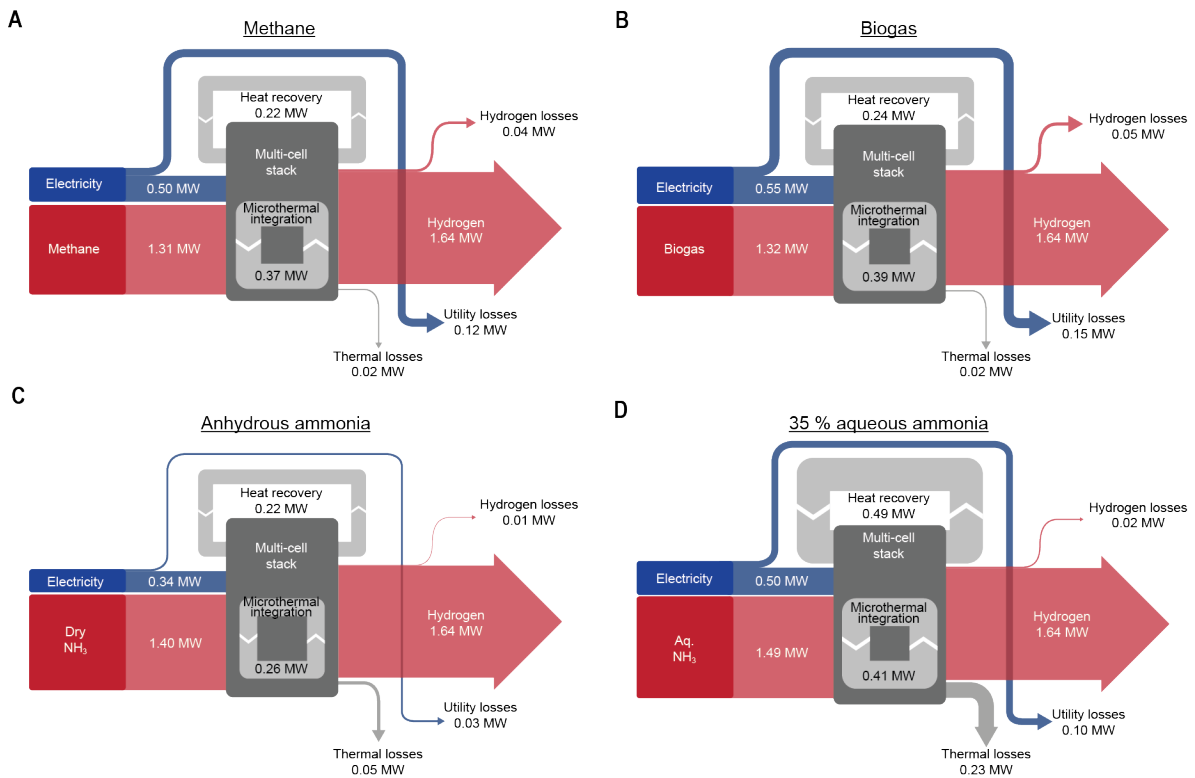
Fig. S15. Sankey diagrams for PCER operation producing 1 ton H₂/day.
PCER operation at 750°C with hydrogen delivery pressure at 26 bar. Electricity input electricity (MW) shows total amount (not subtracting utility losses). (**A**) Methane with methane inlet conditions of 20°C and 29 bar. System efficiency = 90.5% (**B**) Biogas with inlet conditions at 20°C and 1 bar. System efficiency = 88.0%. (**C**) Anhydrous ammonia with liquid ammonia at 6 bar and 8°C as feed. System efficiency = 94.5%. (**D**) 35% aqueous ammonia at atmospheric pressure and temperature as feed. System efficiency = 82.5%. High heating values (HHV) are used for all the fuels, the values are listed in materials and methods. Assumptions can be found in figs. S17 for methane, S18 for biogas, S19 for anhydrous ammonia and S20 for aqueous ammonia.
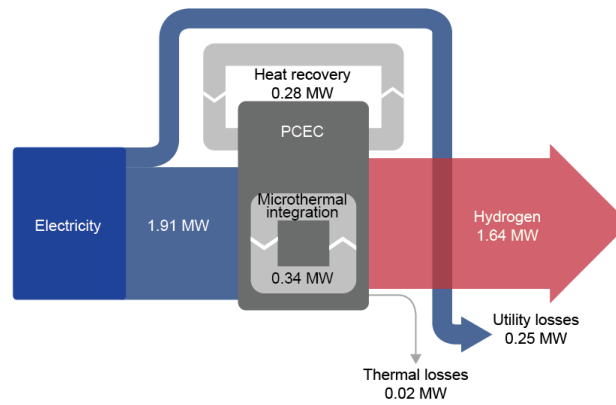
Fig. S16. Sankey diagrams for HT-WEL operation producing 1 ton H₂/day.

Proton conducting electrolysis cell operation at 750°C with hydrogen delivery pressure at 26 bar. Electricity input electricity (MW) shows total amount (not subtracting utility losses). System efficiency = 85.9% (using the higher heating value, HHV, of hydrogen). Using the lower heating value, LHV, of hydrogen, the system efficiency = 72.7 %. Assumptions can be found in fig. S21.
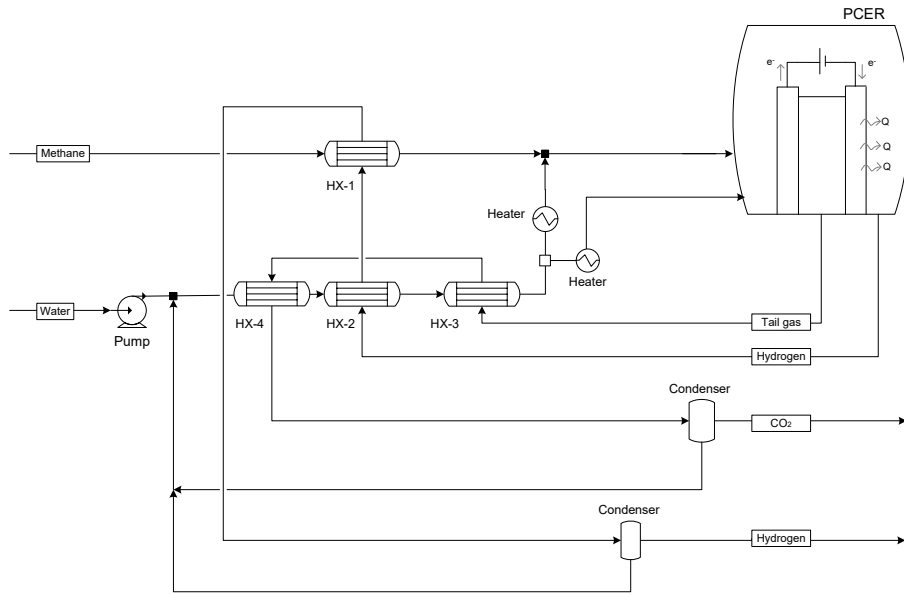
Assumptions for PMR—methane hydrogen production process

Hydrogen recovery	99%
Reforming reaction (PMR)	Reforming at T = 750°C
	Operation pressure = 27.9 bar
	S/C ratio = 2.5
Heat exchanger -1	Methane with Hydrogen
	$\Delta p/p$ = 2%
	Minimum ΔT = 30°C (gas-gas)
Heat exchanger -2	Water with Hydrogen
	$\Delta p/p$ = 2%
	Minimum ΔT = 20°C (Liquid-gas)
Heat exchanger -3	Water with Tail gas
	$\Delta p/p$ = 2%
	Minimum ΔT = 20°C (Liquid-gas)
Heat exchanger -4	Water with Tail gas
	$\Delta p/p$ = 2%
	Minimum ΔT = 20°C (Liquid-gas)
Pump	Efficiency = 90%
	Discharge pressure 29 bar
Condenser H_2	Operation temperature = 50°C
	Operation pressure = 26 bar
	Calculated as flash operation
Condenser CO_2	Operation temperature = 80°C
	Operation pressure = 27 bar
	Calculated as flash operation
Heater Steam inlet	Outlet temperature = 598°C
Heater Steam sweep	Outlet temperature = 750°C

Fig. S17. Process flow diagram and main assumptions and conditions for methane.
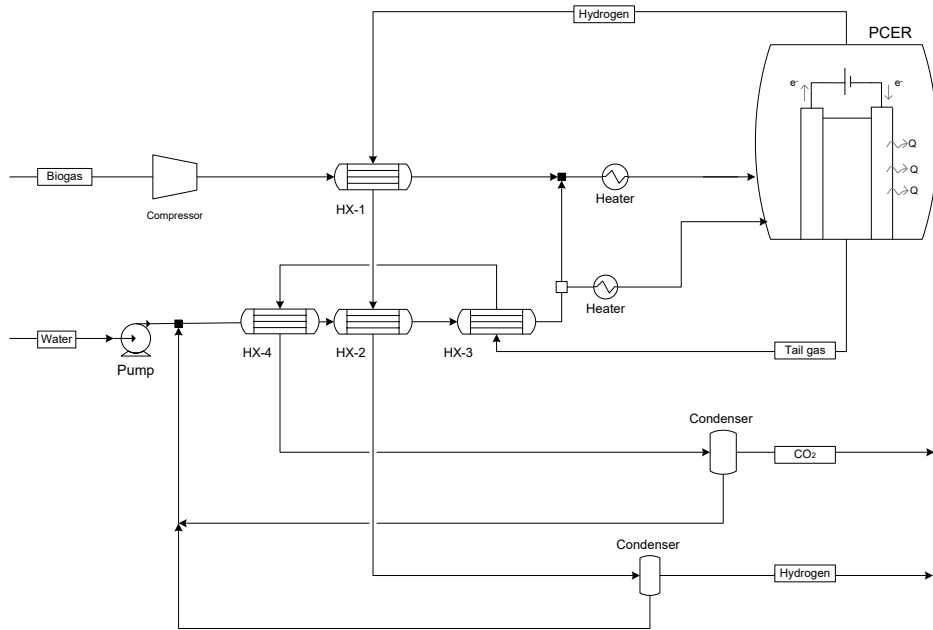
Assumptions for PMR—biogas hydrogen production process

Hydrogen recovery	99%
Reforming reaction (PMR)	Reforming at T = 750°C
	Operation pressure = 27.9 bar
	S/C ratio = 2.5
Heat exchanger -1	Methane with Hydrogen
	$\Delta p/p$ = 2%
	Minimum ΔT = 30°C (gas-gas)
Heat exchanger -2	Water with Hydrogen
	$\Delta p/p$ = 2%
	Minimum ΔT = 20°C (Liquid-gas)
Heat exchanger -3	Water with Tail gas
	$\Delta p/p$ = 2%
	Minimum ΔT = 20°C (Liquid-gas)
Heat exchanger -4	Water with Tail gas
	$\Delta p/p$ = 2%
	Minimum ΔT = 20°C (Liquid-gas)
Pump	Efficiency = 90%
	Discharge pressure 29 bar
Compressor	Isentropic multistage compressor
	Efficiency = 85%
	Discharge pressure 29 bar
Condenser H_2	Operation temperature = 50°C
	Operation pressure = 26 bar
	Calculated as flash operation
Condenser CO_2	Operation temperature = 80°C
	Operation pressure = 27 bar
	Calculated as flash operation
Heater Steam inlet	Outlet temperature = 750°C
Heater Steam sweep	Outlet temperature = 750°C

Fig. S18. Process flow diagram and main assumptions and conditions for biogas.
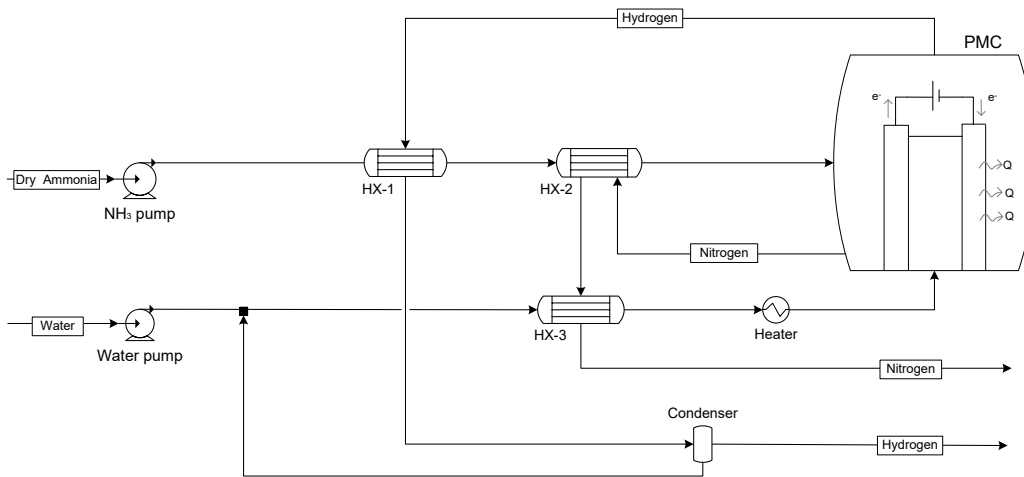
Assumptions for PMR—anhydrous NH₃ hydrogen production process

Hydrogen recovery	99%
Cracking reaction (PMC)	Cracking at T = 750°C
	Operation pressure = 27.9 bar
Heat exchanger -1	Ammonia with Hydrogen
	$\Delta p/p = 2\%$
	Minimum $\Delta T = 50°C$
Heat exchanger -2	Ammonia with Nitrogen
	$\Delta p/p = 2\%$
	Minimum $\Delta T = 30°C$
Heat exchanger -3	Water with Nitrogen
	$\Delta p/p = 2\%$
	Minimum $\Delta T = 20°C$
Condenser H₂	Operation temperature = 50°C
	Operation pressure = 26 bar
	Calculated as flash operation
Water Pump	Efficiency = 90%
	Discharge pressure 29 bar
Ammonia Pump	Efficiency = 90%
	Discharge pressure 29 bar
Heater Steam sweep	Outlet temperature = 750°C

Fig. S19. Process flow diagram and main assumptions and conditions for anhydrous ammonia.
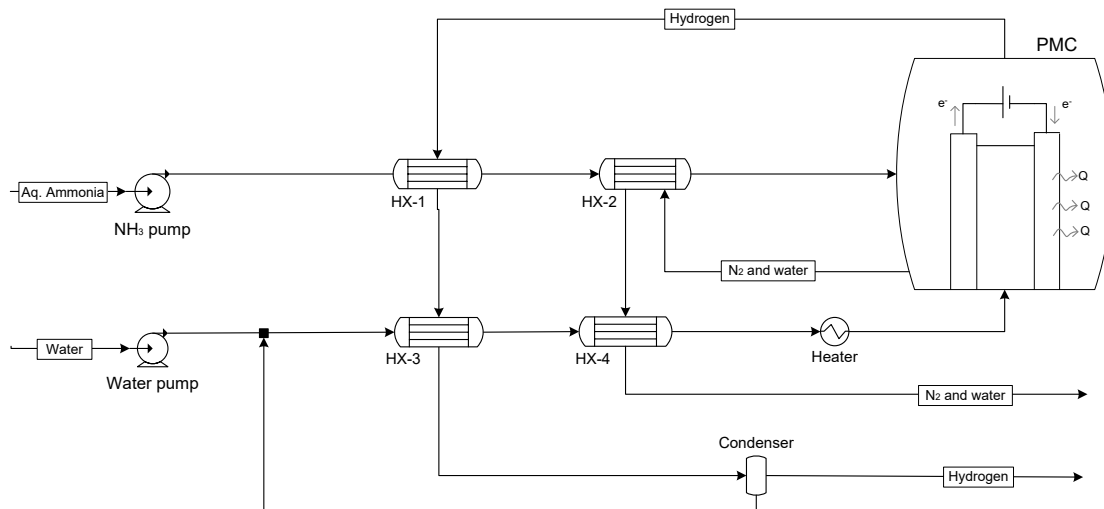
Assumptions for PMR—aqueous NH₃ hydrogen production process	
Hydrogen recovery	99%
Cracking reaction (PMC)	Cracking at T = 75°C
	Operation pressure = 27.9 bar
Heat exchanger -1	Ammonia with Hydrogen
	$\Delta p/p$ = 2%
	Minimum ΔT = 20° C (Liquid-gas)
Heat exchanger -2	Ammonia with Nitrogen + water
	$\Delta p/p$ = 2%
	Minimum ΔT = 20°C
Heat exchanger -3	Water with Hydrogen
	$\Delta p/p$ = 2%
	Minimum ΔT = 20°C
Heat exchanger -4	Water with Nitrogen + water
	$\Delta p/p$ = 2%
	Minimum ΔT = 20°C
Condenser H₂	Operation temperature = 50°C
	Operation pressure = 26 bar
	Calculated as flash operation
Water Pump	Efficiency = 90%
	Discharge pressure 29 bar
Ammonia Pump	Efficiency = 90%
	Discharge pressure 29 bar
Heater Steam sweep	Outlet temperature = 750°C

Fig. **S20. Process flow diagram and main assumptions and conditions for aqueous ammonia.**
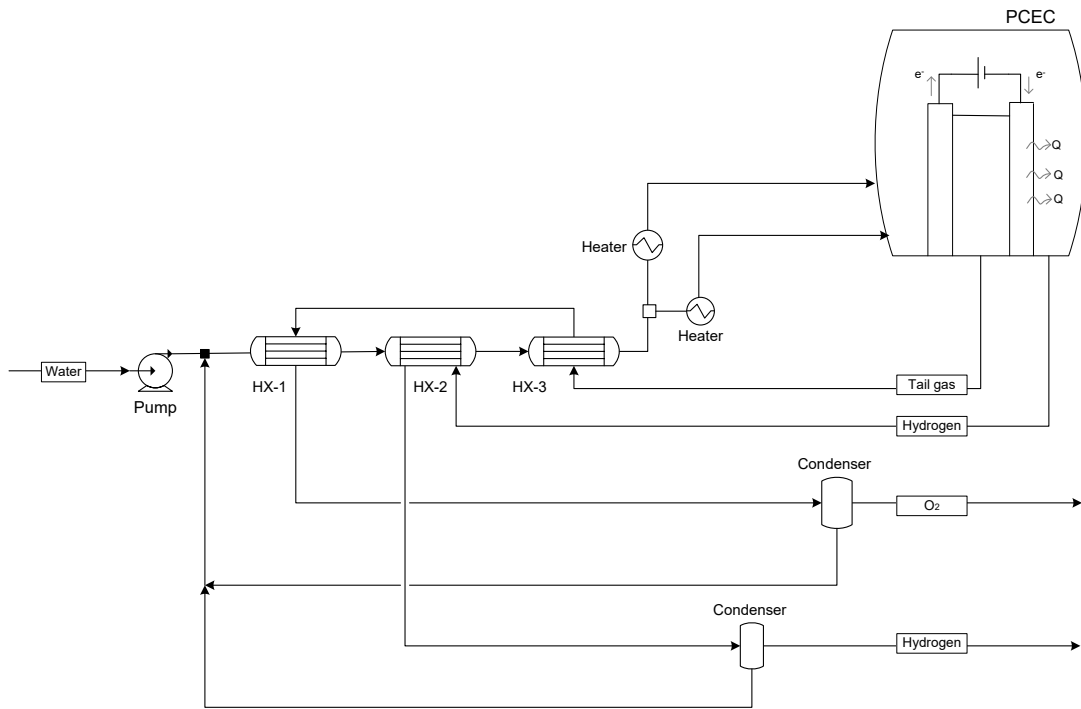
Assumptions for PMR—HT water electrolysis hydrogen production process

|	
Fuel utilization (%Steam)	80%
Water Electrolysis	Operation Temperature = 750°C
	Operation pressure = 27.9 bar
	Faraday efficiency = 95%
Heat exchanger -1	Tail gas with water
	Δp/p = 2%
	Minimum ΔT = 20°C(liquid-gas)
Heat exchanger -2	Water/steam with Hydrogen
	Δp/p = 2%
	Minimum ΔT = 20°C (liquid-gas)
Heat exchanger -3	Water/steam with Tail gas
	Δp/p = 2%
	Minimum ΔT = 30°C (Liquid/gas-gas)
Pump	Efficiency = 90%
	Discharge pressure 29 bar
Condenser H_2	Operation temperature = 50°C
	Operation pressure = 26 bar
	Calculated as flash operation
Condenser O_2	Operation temperature = 40°C
	Operation pressure = 27 bar
	Calculated as flash operation
Heater Steam inlet	Outlet temperature = 450°C
Heater Steam sweep	Outlet temperature = 750°C

Fig. S21. Process flow diagram and main assumptions and conditions for HT-WEL.
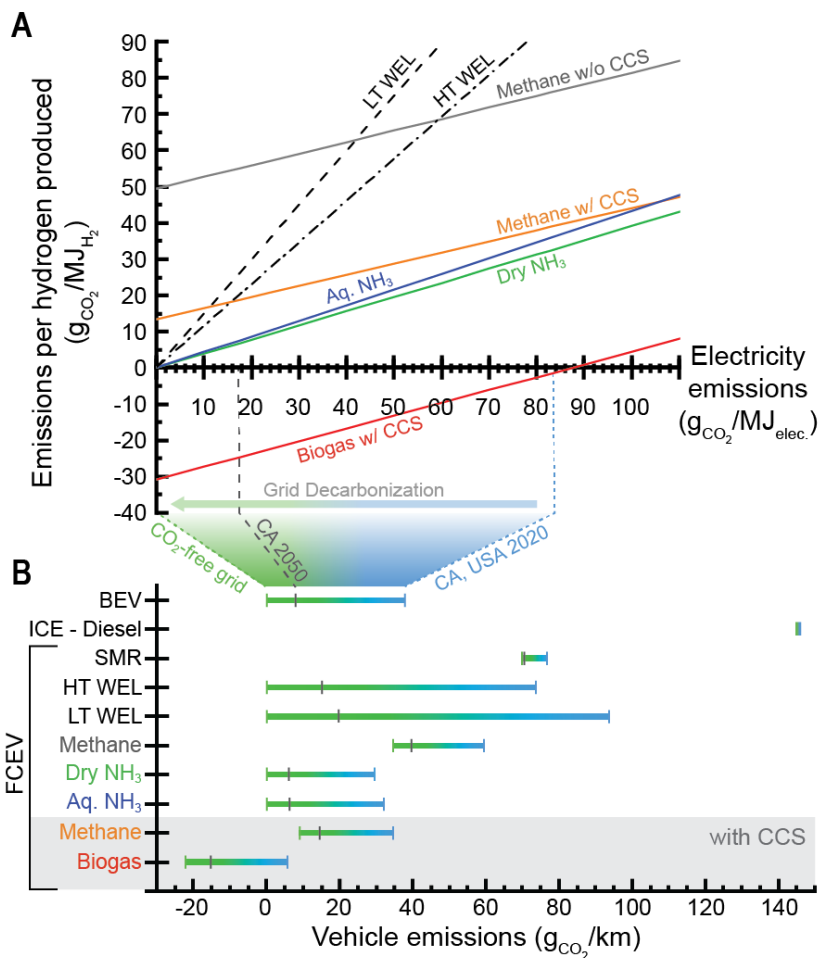
Fig. S22. CO₂ emission comparisons.

(**A**) Carbon emissions for produced hydrogen (g_{CO2}/MJ_{H2}) with PCERs from methane (with and without CCS), biogas with CCS, anhydrous and aqueous ammonia and also for high-temperature steam electrolysis (HT WEL; proton-conducting) and low-temperature water electrolysis (LT WEL; alkaline) as a function of grid electricity carbon emissions (g_{CO2}/MJ_{elec}). LT WEL is a mature technology with efficiency assumptions listed in fig. S23, while HT WEL is an example of a future, more efficient electrolysis technology with underlying energy efficiency analysis set out in fig. S16 and based on flow sheet in fig. S21, which uses comparable methodology to the energy efficiency analysis for PCERs in fig. S15 based on flow sheets in figs. S17 to S20. (**B**) Vehicle emission ranges (well-to-wheel) for California 2020 (blue) and zero-emission grid (green) with California 2050 targets indicated in grey. Emissions given by grid electricity carbon emissions for hydrogen produced using proton ceramic electrochemical reactors (PCERs) using methane (with and without CCS), biogas (with and without CCS), and ammonia, compared with BEVs and ICEs. Grid electricity carbon emissions highlighted in (**A**) are used for the vehicle emission calculations. For details see fig. S23 and table S1.
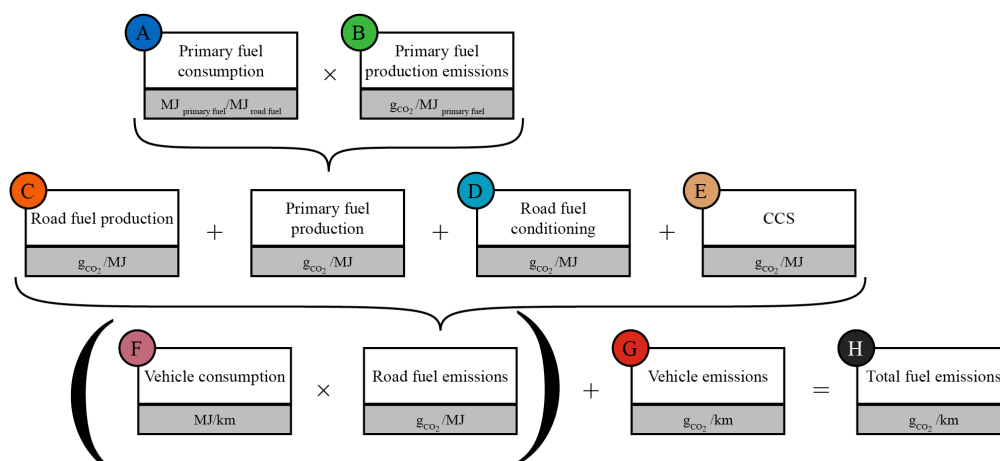
	A, $MJ_{primary\ fuel}/MJ_{road\ fuel}$	**B**, $g_{CO_2}/MJ_{primary\ fuel}$			**C**, g_{CO_2}/MJ			**D**, g_{CO_2}/MJ		
	2020, 2050 and ZE	2020	2050	ZE	2020	2050	ZE	2020	2050	ZE
H2 Vehicle (PCER) Methane	NG: 0.80 EL: 0.31	NG: 15.30 EL: 82.92	NG: 15.30 EL: 17.50	NG: 15.30 EL: 0	37.3	37.3	37.3	10.51	2.22	0
Dry NH3	Dry NH3: 0.85 EL: 0.17	Dry NH3: 3.96 EL: 82.92	Dry NH3: 0.84 EL:17.50	Dry NH3: 0 EL: 0	0	0	0	10.51	2.22	0
Aq. NH3	Aq NH3: 0.91 EL: 0.30	Aq NH3: 11.74 EL: 82.92	Aq NH3: 2.48 EL:17.50	Aq NH3:0 EL: 0	0	0	0	10.51	2.22	0
Methane with CCUS	NG: 0.80 EL: 0.31	NG: 15.30 EL: 82.92	NG: 15.30 EL: 17.50	NG: 15.30 EL: 0	0.37	0.37	0.37	10.51	2.22	0
Biogas with CCUS*	Biogas: 0.80 EL: 0.33	Biogas: 10.26 EL: 82.92	Biogas: 10.26 EL:17.50	Biogas: 10.26 EL: 0	0.63	0.63	0.63	10.51	2.22	0
H2 Vehicle HT WEL	EL: 1.15	EL: 82.92	EL: 14.09	EL: 0	0	0	0	10.51	2.22	0
LT WEL	EL: 1.50*	EL: 82.92	EL: 14.09	EL: 0	0	0	0	10.51	2.22	0

	(A x B)+C, g_{CO_2}/MJ		D, g_{CO_2}/MJ		
	2020	2050	2020	2050	ZE
H2 Vehicle SMR	99.43*	99.43*	10.51	2.22	0
BEV	82.92	14.09	0	0	0
ICE-Diesel	25.59*	25.09*	0	0	0

|	**E**, g_{CO_2}/MJ			**F**, MJ/km			**G**, g_{CO_2}/km	**H, Total vehicle emissions**, g_{CO_2}/km		
	2020	2050	ZE	2020	2050	ZE		**2020**	**2050**	**ZE**
H2 Vehicle (PCER) Methane	0	0	0	69.7	69.7	69.7	0	**59.70**	**39.82**	**34.52**
Dry NH3	0	0	0	69.7	69.7	69.7	0	**29.91**	**6.31**	**0.00**
Aq. NH3	0	0	0	69.7	69.7	69.7	0	**32.34**	**6.82**	**0.00**
Methane with CCUS	1.55	0.82	0	69.7	69.7	69.7	0	**34.95**	**14.64**	**8.77**
Biogas with CCUS*	2.61	1.39	0	69.7	69.7	69.7	0	**6.10**	**-15.75**	**-40.90**
H2 Vehicle HT WEL	0	0	0	69.7	69.7	69.7	0	**74.02**	**15.62**	**0.00**
LT WEL	0	0	0	69.7	69.7	69.7	0	**93.90**	**19.82**	**0.00**

	E, g_{CO_2}/MJ			**F**, MJ/km			**G**, g_{CO_2}/km	Total vehicle emissions, g_{CO_2}/km		
	2020	2050	ZE	2020	2050	ZE		**2020**	**2050**	**ZE**
H2 Vehicle SMR	0	0	0	69.7	69.7	69.7	0	**76.96**	**71.18**	**69.63**
BEV	0	0	0	45.7	45.7	45.7	0	**37.86**	**7.99**	**0.00**
ICE-Diesel	0	0	0	145.5	145.5	74.86	74.86	**146.14**	**145.43**	**144.56**

Fig. S23. Methodology scheme for CO₂ emission calculation in fig. S22.
Values for calculating total vehicle emissions for California 2020, California 2050 target, and zero-emission (ZE) scenarios. See table S1 for details on assumptions and references.
*Corrected with carbon credit.
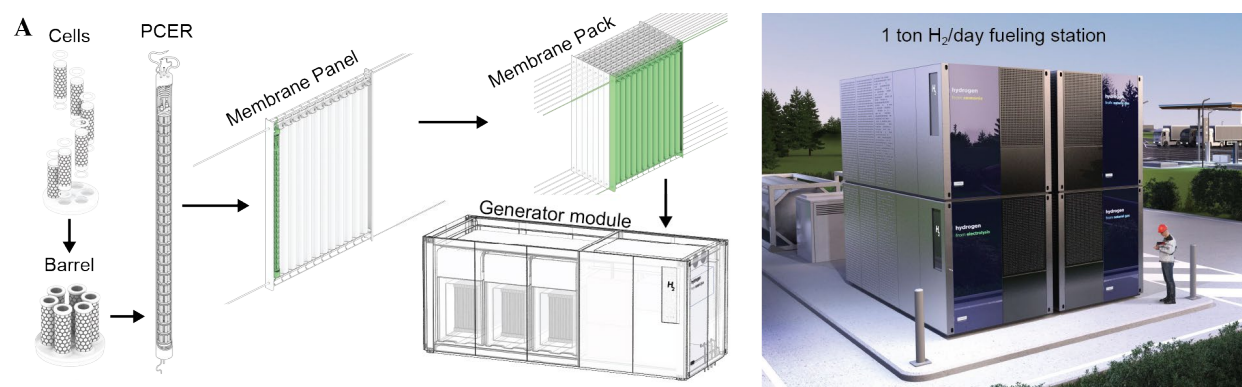
B, Build-up from electrochemical cells to hydrogen generator

Ceramic stack		Reactor shell		Membrane panel		Membrane pack		Generator module	
Cell length:	25 mm	Height:	900 mm	Stacks:	12	Panels:	8	Packs:	3
Cell O.D.:	9.6 mm	Material:	EN 1.4959	Total volume:	12.3 L	Total stacks:	96	Total stacks:	288
Parallel cells:	6	Tube O.D.:	47 mm	Total area:	1.3 m^2	Total area:	10.4 m^2	Total area:	31.1 m^2
Serial ICs:	24	Wall:	2.8 mm			Nom. area[1]:	8.6 m^2	Nom. area[1]:	25.9 m^2
Total cells:	144								
Total area:	0.108 m^2								

[1]Nominal area is typical productive area with allowance for 1 panel per pack to shut-off and additional 5% of cells to disconnect as degradation.

C, Hydrogen production rates

	Current density (A/cm^2)				Production rate per membrane area (kg/day/m^2)			
	Methane	Biogas	Dry NH$_3$	Aq. NH$_3$	Methane	Biogas	Dry NH$_3$	Aq. NH$_3$
Max[1]		1.40				12.62		
Nominal[2]		1.20				10.72		
Lean[3] @ 0.6 Ω cm^{-2}	0.45	0.45	0.39	0.52	4.06	4.05	3.52	4.67
Lean[4] @ 0.2 Ω cm^{-2}	1.36	1.36	1.17	1.40	12.18	11.12	10.59	12.62

[1]Max current density for peak operation limited by current collection in stack. [2]Nominal current density for sustained operations. [3]Highest energy efficiency for early generation of membranes with total area specific resistance (ASR) of 0.6 Ω cm^2. [4]Highest energy efficiency operations for later generations of membranes (reference (25) for report ASR of 0.09 Ω cm^2 for a proton conducting cell at 600°C).

D, Raw materials consumption

		RTY[1] %	Stack total g	Module total kg	Per area kg/m^2	Per H$_2$ capacity[2] kg/(kg$_{H2}$/day)
Ceramic stack	BaSO$_4$	42.3	462	133	4.3	0.48
	ZrO$_2$	42.3	68	20	0.6	0.07
	CeO$_2$	42.3	171	49	1.6	0.18
	Y$_2$O$_3$	42.3	22	6	0.2	0.02
	NiO	42.3	1023	295	9.5	1.05
	Quartz sand	57.8	250	72	2.3	0.26
	MgO	67.2	76	22	0.7	0.08
	CaCO$_3$	57.6	172	50	1.6	0.18
	Al$_2$O$_3$	64.4	81	23	0.7	0.08
	Cu	100	256	74	2.4	0.26
	Ni	56.2	294	85	2.7	0.30
	Sub-total		2876	828	27	3.0
Reactor shell	EN 1.4959	100	3056	880	28.3	3.1
	EN 1.4541	100	256	74	2.4	0.3
	Sub-total		3313	954	31	3.4

[1]Rolled throughput yield from stack manufacturing. [2]Nominal capacity (nominal current density x nominal area).

Fig. S24. Conceptual design for estimate of raw materials consumption.

(**A**) Illustration of conceptual design of hydrogen fueling station built up from electrochemical cells to hydrogen generator modules and 1 ton H$_2$/day fueling station. (**B**) Geometrical specifications and assumptions for the build-up from cell to module. (**C**) Hydrogen production rates for design envelope current densities where "lean" values are calculated using models disclosed under figs. S17 to S21 and Methods. (**D**) Raw materials consumption required to build the hydrogen generators under assumption of nominal current density and area calculations.
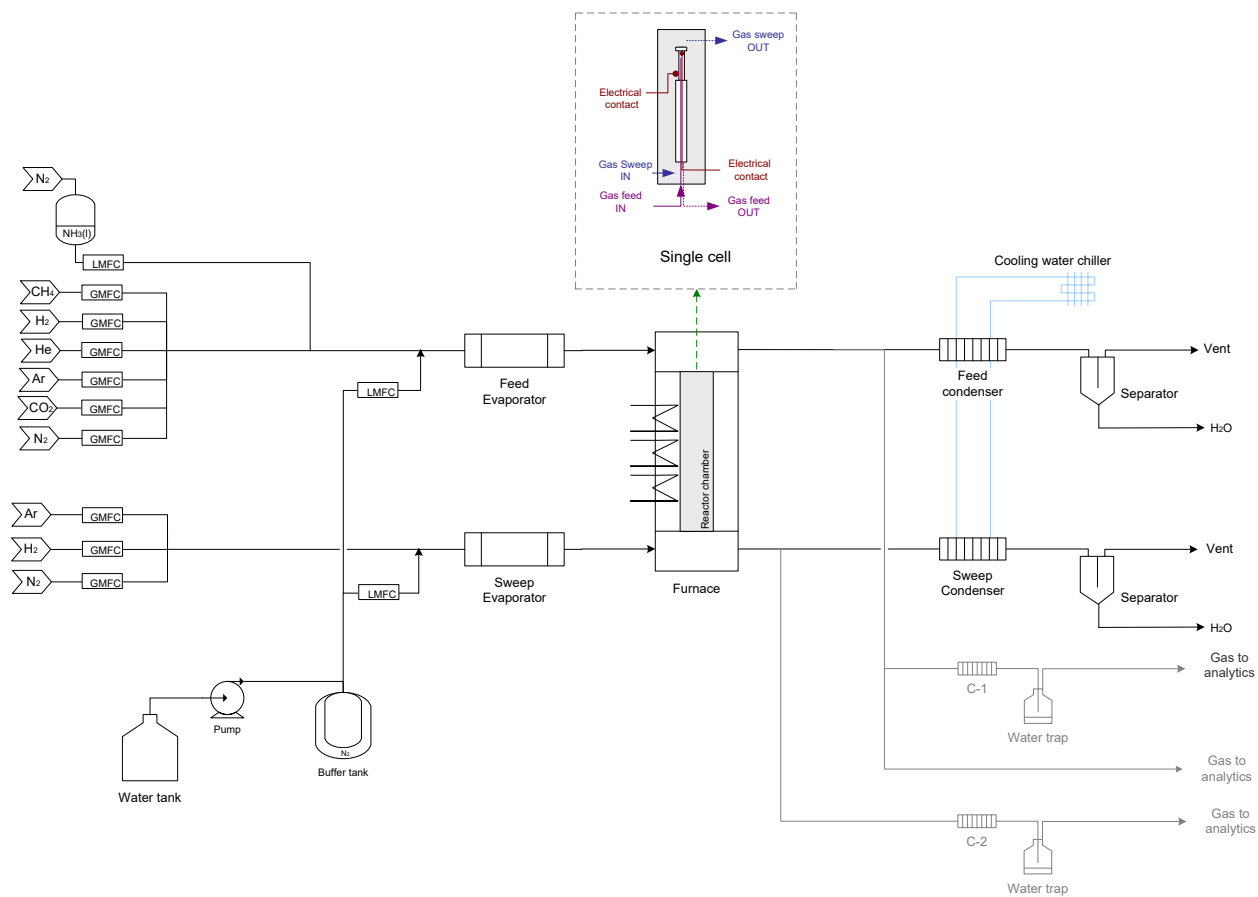
Fig. S25. Process flow diagram for single cell reactor set-up.
GMFC: Gas mass flow controller. LFMC: Liquid mass flow controller.
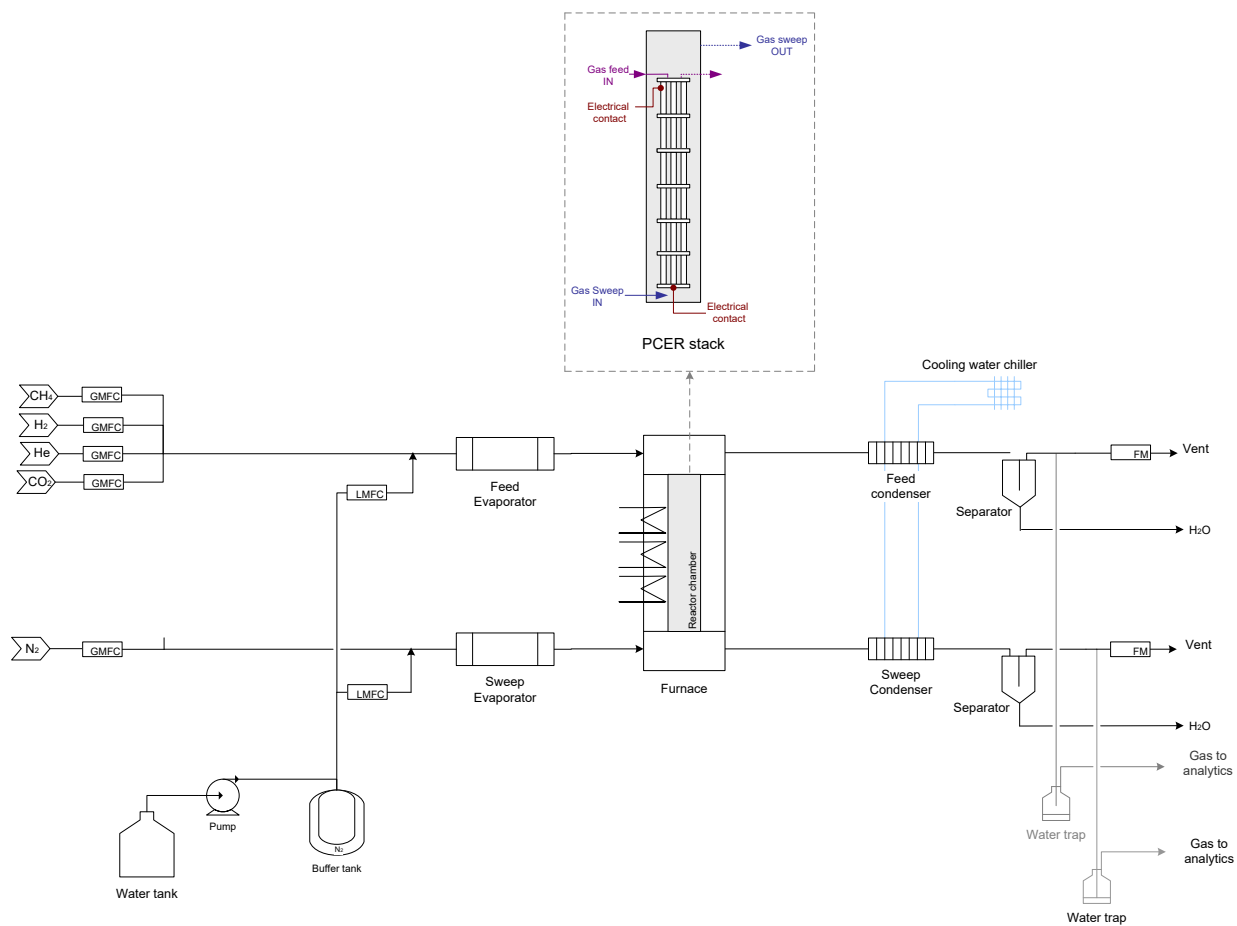
Fig. S26. Process flow diagram of test rig used for PCER stack testing.
GMFC: Gas mass flow controller. LFMC: Liquid mass flow controller. FM: Flow meter.
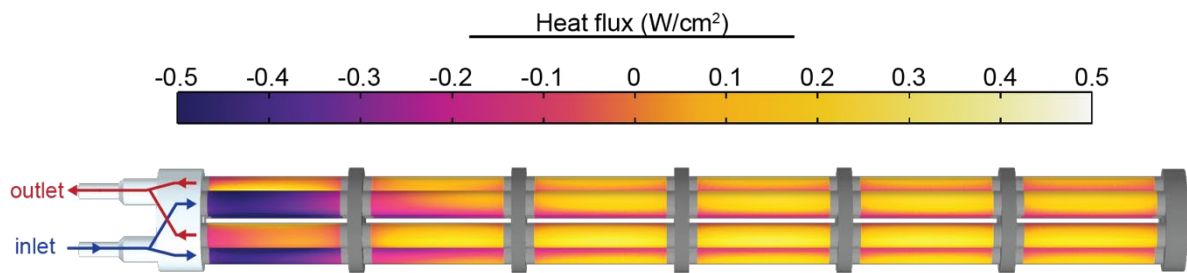
Fig. S27. PCER stack heat flux.
Outward normal heat flux (W/cm^2), calculated from the multiphysics model for methane fuel at 750°C, 20 bar, S/C = 2.5, 0.61 A/cm^2, 0.30 kg/day H$_2$. The sign of the heat flux indicates if heat is flowing into or out from the cells: A negative heat flux means that heat is flowing into the cell, whereas a positive heat flux means heat flows out from the cell. A net endothermic cell has a negative heat flux, meaning heat is absorbed by the cell, with the opposite being true for net exothermic cells. In endothermic cells the heat absorbed by endothermic reactions is higher than the heat produced by the galvanostatic membrane operation and hydrogen compression. As is seen in particular for the topmost (left) barrel, the adjacency of net endothermic and exothermic cells allows for heat transfer between them for thermally balanced operation of the PCER.
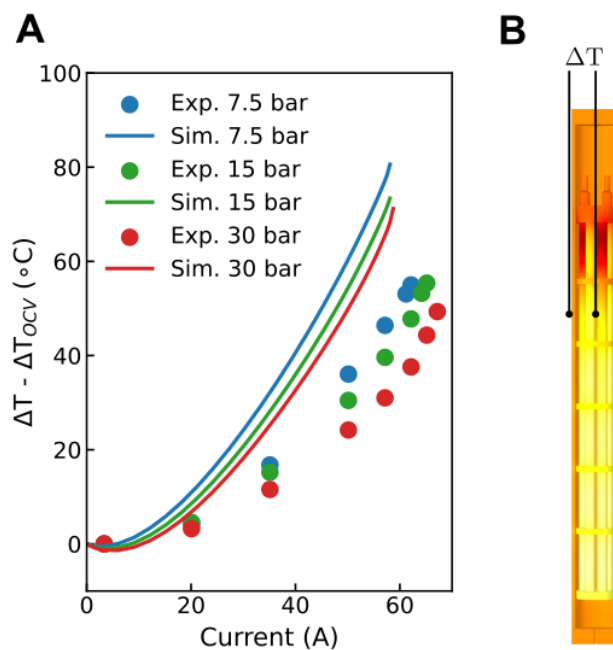
Fig. S28. Comparison of model and experimental data.
(**A**) Difference between internal and external temperature adjusted for the OCV value (0A).
(**B**) Position of thermocouples placed in the PCER stack. The simulated and experimental
temperature differences show the same pressure dependency, where temperature differences
are lower at higher pressures. One reason for this is the increase in thermal conductivity of
gases with pressure. The comparison of model and experiment data indicate that the PCER
has more efficient heat transfer from the external shell side to the internal stack than what is
captured by the model. Radiative heat transfer is not considered in the model but would
improve the heat transfer and reduce the temperature differences in the simulated results. The
offset between experimental and modeled currents is due to a faradaic efficiency <100% in
the experiments.

A

$$CH_4 + H_2O \rightleftarrows CO + 3\,H_2 \qquad \text{M1}$$

$$CO + H_2O \rightleftarrows CO_2 + H_2 \qquad \text{M2}$$

$$CH_4 + H_2O \rightleftarrows CO_2 + 4\,H_2 \qquad \text{M3}$$

$$CH_4 + CO_2 \rightleftarrows 2\,CO + 2\,H_2 \qquad \text{B1}$$
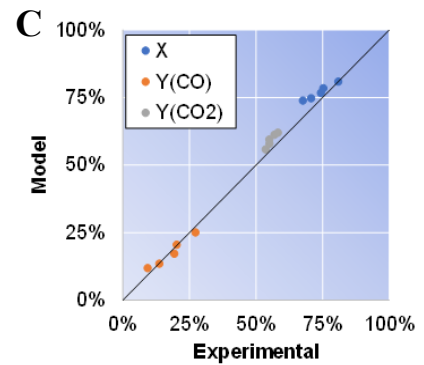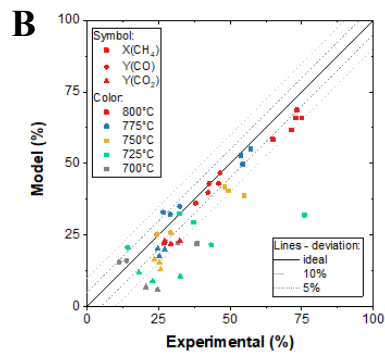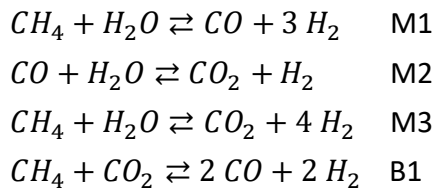
Fig. S29. Kinetic study for methane and biogas steam reforming.

(**A**) Considered reaction network; (**B**) Parity plot (model vs. experimental results) corresponding to X(CH$_4$), Y(CO) and Y(CO$_2$) by fitting experimental results obtained from SMR experimental tested; and (**C**) Parity plot for biogas reforming kinetic fitting including the addition B1 reaction (dry reforming).

Fig. S30. PCER electrode material stability under high H₂ recoveries.

Evolution of H_2, CH_4, CO and CO_2 molar fractions in dependence of time during the reduction-oxidation cycles at 800ºC.

Table S1.

List of literature interconnect coefficient of thermal expansions (CTEs) and conductivities presented in fig. S5.

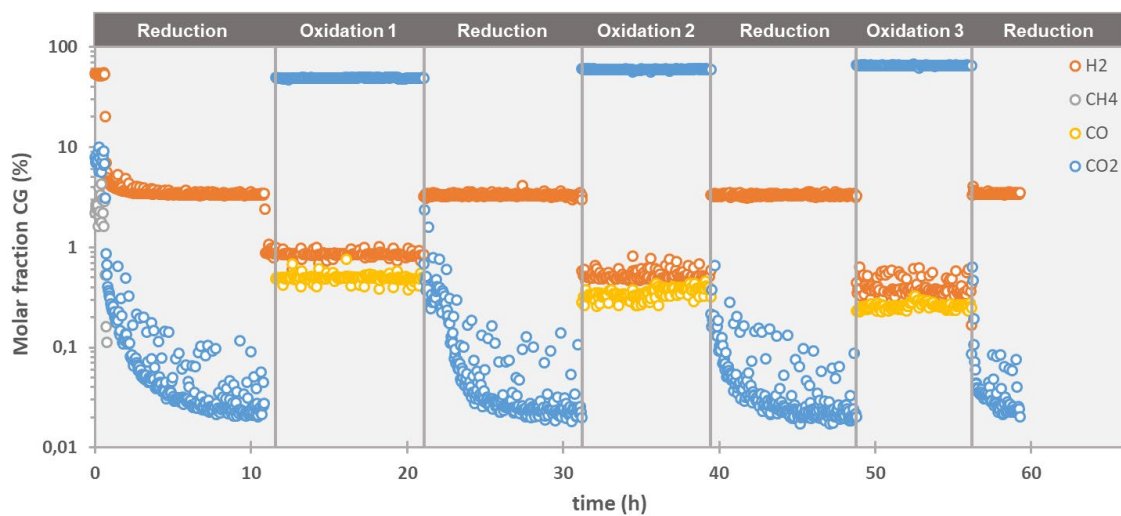| Composition/Commercial Name	Electrical conductivity S/cm (800°C)	CTE x 10^{-6} K^{-1} (800°C)	Reference
Crofer 22 H	9.20E+03	11.80	(26)
Crofer 22 APU	8.70E+03	11.90	(27)
$MgAl_2O_4$	1.00E-06	9.00	(28)
$MnAl_2O_4$	1.00E-03	7.90	
$CoAl_2O_4$	1.00E-07	8.70	
$NiAl_2O_4$	1.00E-04	8.10	
$ZnAl_2O_4$	1.00E-06	8.70	
$MgCr_2O_4$	2.00E-02	7.20	
$MnCr_2O_4$	2.00E-02	6.80	
$CoCr_2O_4$	2.00E-02	8.20	
$NiCr_2O_4$	7.30E-01	7.30	
$ZnCr_2O_4$	1.00E-02	7.10	
$MgMn_2O_4$	9.70E-01	8.70	
Mn_3O_4	1.00E-01	8.80	
$CoMn_2O_4$	9.70E-01	8.70	
$NiMn_2O_4$	1.40E+00	8.60	
$Cu_{1.3}Mn_{1.7}O_4$	225 (750°C)	12.20	
$MgFe_2O_4$	8.00E-02	12.30	
$MnFe_2O_4$	8.00E+00	12.50	
$CoFe_2O_4$	9.30E-01	12.10	
$NiFe_2O_4$	2.60E-01	10.80	
$CuFe_2O_4$	9.10E+00	11.20	
$ZnFe_2O_4$	7.00E-02	7.00	
$MnCo_2O_4$	6.00E+01	9.70	
Co_3O_4	6.70E+00	9.30	
$CuCo_2O_4$	2.75E+01	11.40	
Haynes 242 (Ni-MoCr superalloy)	7.50E+03	14.00	(29)
Haynes 23 (Ni-based)	7.70E+03	15.20	
$LaCrO_3$	0.34 (700°C), 1 (1000°C)	9.50	(30)
$LaCr_{0.9}Mg_{0.1}O_3$	3 (1000°C)	9.50	
$La_{0.9}Sr_{0.1}CrO_3$	14 (1000)	10.70	
Cr_2O_3	1.00E-02	9.6 (1000°C)	
MgO	5.56E-08	15.6 (1000°C)	
Ducrolloy (Cr-based)	1.00E+04	11.8–12	(31)
Silver (99,9%)	1.60E+05	18.9–22	
Nickel	2.50E+04	12–13.5	
Platinum	2.30E+04	10.00	
Gold	1.10E+05	16.60	
Palladium	2.55E+04	12.30	
$MnCo_2O_4$	3.40E+01	12.30	(32)
$Mn_{1.5}Co_{1.5}O_4$	3.10E+01	10.60	(33)
$MnCu_{0.5}Co_{1.5}O_4$	105.5 (750°C)	12.3 (1000°C)	(34)
$LaCrO_3$	9.60E-01	11.3 (1000°C)	(35)
$La_{0.7}Mg_{0.3}CrO_3$	3.35E+00	9.9 (1000°C)	
$La_{0.7}Ca_{0.3}CrO_3$	5.01E+01	11.5 (1000°C)	
$La_{0.7}Ba_{0.3}CrO_3$	2.69E+00	12.5 (1000°C)	
$La_{0.75}Sr_{0.25}CrO_3$	5.91E+01	11.6 (1000°C)	
$La_{0.75}Sr_{0.25}Cr_{0.5}Mn_{0.5}O_3$	2.88E+01	12 (1000°C)	

Table S2. Carbon emission values and assumptions and references used in fig. S22 and S23.

B, Primary fuel emissions

Parameter	Value	Comment on reference	Reference
California (CA) 2020 **electricity** emissions	82.92 g_{CO2}/$MJ_{elec.}$	Page 2. Table 1: Fuel pathway code: ELC000L00072020.	(36)
Target CA 2050 **electricity** emissions	17.5 g_{CO2}/$MJ_{elec.}$ (0.063 kg_{CO2}/$kWh_{elec.}$)	Page G-3. Table G-1 (2050). Based on CA executive order B-30-15.	(37)
Methane emissions	15.30 g_{CO2}/MJ	Page 18. Table C.1 Compressed NG vehicle, excluding compression and tailpipe emissions. Upstream methane leakage emissions are included in accordance with the CA GREET model assumptions.(Page 21. Table C.3)	(16)
Biogas emissions	10.26 g_{CO2}/MJ	Page 37. Table F.3 Biomethane emissions excluding processing for upgrading.	(16)
Dry NH$_3$ emissions 2020	3.96 g_{CO2}/MJ	Green ammonia production. Emissions only related to transportation. Transportation emissions calculated based on ethanol transportation emissions (3 g_{CO2}/MJ, APPENDIX A Figure A-1) and adjusted for the ratio between energy content in ethanol and dry NH$_3$. Emissions is assumed to decrease linearly from 2020 grid emissions (82.92 g_{CO2}/$MJ_{elec.}$) towards zero grid emission intensity.	(38)
Aq. NH$_3$ emissions 2020	11.74 g_{CO2}/MJ	Green ammonia production. Emissions only related to transportation. Transportation emissions calculated based on ethanol transportation emissions (3 g_{CO2}/MJ, APPENDIX A Figure A-1) and adjusted for the ratio between energy content in ethanol and dry NH$_3$. Emissions is assumed to decrease linearly from 2020 grid emissions (82.92 g_{CO2}/$MJ_{elec.}$) towards zero grid emission intensity.	(38)

D, Hydrogen conditioning

Parameter	Value	Comment on reference	Reference
H$_2$ compression and cooling emissions 2020	10.51 g_{CO2}/MJ	Page 37. Table F.3.	(16)
H$_2$ compression and cooling emissions 2050	2.22 g_{CO2}/MJ	78,89 % reduction has been applied from 2020 emissions.	

E, CCUS to liquid CO$_2$

Parameter	Value	Comment on reference	Reference
Liquefaction energy required	0.3 MJ/kg_{CO2}	Assuming a CO2 concentration higher than 80 % in tail gas	(39)
CO$_2$ Captured %	99%	A small fraction off the off-gas from liquefaction is purged, amounting to 1 % of CO$_2$	
CO$_2$ transportation emissions 2020, % of captured	1.7%	Assumed no loss of CO$_2$ during transport (no boil-off) and transport by ship (1000 km).	(40)
CO$_2$ transportation emissions 2050, % of captured	1.7%	Assumed no loss of CO$_2$ during transport (no boil-off) and transport by ship (1000 km).	(40)

F, Vehicle consumption

Parameter	Value	Comment on reference	Reference
Hydrogen fuel cell vehicle (FCEV)	69.73 MJ/100 km	Page 32. Table 5-11. 2015 case, driving range of 500 km (see page 7, Table 3-4).	(41)
BEV	45.66 MJ/100 km	Page 31. Table 5-10. 2015 case, driving range of 150 km (see page 7, Table 3-4).	(41)
Diesel-ICE	145.49 MJ/100 km	Page 30. Table 5-6. 2015 case. See section 3.3.1 for vehicle specifications.	(41)

G, Vehicle emissions

Parameter	Value	Comment on reference	Reference
Only Diesel-ICE	74.86 g_{CO2}/km	Page 11. Table B1.	(16)

Table S3. Model equations for multiphysics model.

Physics	Model	Equation	Nomenclature	
Fluid flow	Navier-Stokes equations (free gas flow)	$\rho(\mathbf{u}\cdot\nabla)\mathbf{u} = \nabla\cdot[-p\mathbf{I}+\mathbf{K}]$ $\nabla\cdot(\rho\boldsymbol{u})=0$ $\mathbf{K}=\mu(\nabla\mathbf{u}+(\nabla\mathbf{u})^{\mathrm{T}})-\dfrac{2}{3}\mu(\nabla\cdot\mathbf{u})\mathbf{I}$	ρ	Mixture density
			$\mathbf{u}$	Velocity vector
	Brinkman equations (porous media gas flow)	$\dfrac{1}{\epsilon_p}\rho(\mathbf{u}\cdot\nabla)\mathbf{u}\dfrac{1}{\epsilon_p}=\nabla\cdot[-p\mathbf{I}+\mathbf{K}]-\mathrm{F_B}$ $\mathrm{F_B}=\left(\mu\kappa^{-1}+\beta\epsilon_p\rho|\mathbf{u}|+\dfrac{Q_m}{\epsilon_p^2}\right)\mathbf{u}$ $\nabla\cdot(\rho\boldsymbol{u})=Q_m$ $\mathbf{K}=\mu\dfrac{1}{\epsilon_p}(\nabla\mathbf{u}+(\nabla\mathbf{u})^{\mathrm{T}})-\dfrac{2}{3}\mu\dfrac{1}{\epsilon_p}(\nabla\cdot\mathbf{u})\mathbf{I}$	p	Local pressure
			μ	Mixture dynamic viscosity
			ϵ_p	Porosity
			κ	Permeability
			Q_m	Mass source
Mass transfer	Mixture-averaged species transport	$\nabla\cdot\mathbf{j}_i+\rho(\mathbf{u}\cdot\nabla)\omega_i=R_i$ $\mathbf{j}_i=-\left(\rho D_i^m\nabla\omega_i+\rho\omega_i D_i^m\dfrac{\nabla M_n}{M_n}-\mathbf{j}_{\mathrm{c},i}\right)$ $\mathbf{j}_{\mathrm{c},i}=\rho\omega_i\sum_k\dfrac{M_i}{M_n}D_k^m\nabla x_k$	Species $i\in\begin{cases}[CH_4,CO,CO_2,H_2,H_2O]\\ [NH_3,N_2,H_2,H_2O]\\ [H_2,H_2O]\ (\text{sweep})\end{cases}$	
			ω_i	Species mass fraction
	Species averaged diffusivity	$D_i^m=\dfrac{1-\omega_i}{\Sigma_{k\neq i}\frac{x_k}{D_{ik}}}$ $D_{e,ik}=\left(\dfrac{1}{\epsilon_p}\right)^{-\frac{3}{2}}D_{ik},\ \ \text{porous media}$	R_i	Species mass source
			x_k	Species mole fraction
			D_{ik}	Maxwell-Stefan diffusivity
			M_i	Species molar mass
	Mean molecular weight	$M_n=\left(\sum_i\dfrac{\omega_i}{M_i}\right)^{-1}$	R	Universal gas constant $=8.3145\,J\cdot mol^{-1}\cdot K^{-1}$
	Ideal gas law	$\rho=\dfrac{pM_n}{RT}$	T	Local absolute temperature
	Membrane H_2 flux	$-\mathbf{n}\cdot(\mathbf{j}_{H_2}+\rho u_s\omega_{H_2}\mathbf{n})=M_{H_2}R_{H_2}$ $\rho u_s=\mathbf{n}\cdot(\mathbf{j}_{H_2}+\rho u_s\omega_{H_2}\mathbf{n})$ $R_{H_2}=\dfrac{i_{mem}}{2F}$	u_s	Stefan velocity
			i_{mem}	Local membrane normal current density
			F	Faraday constant $=96485\,C\cdot mol^{-1}$
Chemical reaction kinetics	Reaction rate	$r_{j\in M1,M2,M3,B1}=\dfrac{k_j\chi_j}{\zeta^2}$ $r_{j=A1}=\dfrac{k_j\xi_{A1}\chi_j}{\lambda_{A1}}$	Chemical reactions: M1: $CH_4+H_2O\leftrightarrow CO+3H_2$ M2: $CO+H_2O\leftrightarrow CO_2+H_2$ M3: $CH_4+2H_2O\leftrightarrow CO_2+4H_2$ B1: $CH_4+CO_2\leftrightarrow 2CO+2H_2$ A1: $2NH_3\leftrightarrow N_2+3H_2$	
	Arrhenius equation	$k_j=k_j^0 A_{BET}\exp\left(-\dfrac{E_{a,j}}{RT}\right)$	r_j	Local rate of reaction $j\in M1,M2,M3,B1,A1$
	Equilibrium constraints	$\chi_{M1}=\dfrac{p_{CH_4}p_{H_2O}}{p_{H_2}^{2.5}}-\dfrac{p_{H_2}^{0.5}p_{CO}}{K_{eq,M1}}$ $\chi_{M2}=\dfrac{p_{CO}p_{H_2O}}{p_{H_2}}-\dfrac{p_{CO_2}}{K_{eq,M2}}$ $\chi_{M3}=\dfrac{p_{CH_4}p_{H_2O}^2}{p_{H_2}^{3.5}}-\dfrac{p_{H_2}^{0.5}p_{CO_2}}{K_{eq,M3}}$ $\chi_{B1}=p_{CH_4}p_{CO_2}-\dfrac{p_{H_2}^2p_{CO}^2}{K_{eq,B1}}$ $\chi_{A1}=1-\dfrac{p_{N_2}p_{H_2}^3}{K_{eq,A1}p_{NH_3}^2}$	k_j^0	Pre-exponential kinetic coefficient for reaction j
			A_{BET}	BET specific surface area of catalyst (Ni cermet support)
			$E_{a,j}$	Activation energy for reaction j
			χ_j	Equilibrium expression for reaction j
	Adsorption term	$\zeta=1+\dfrac{K_{ads,H_2O}p_{H_2O}}{p_{H_2}}+\Sigma_{i\neq H_2O}K_{ads,i}p_i$	p_i	Dimensionless partial pressure for species i normalized to 1 atm
	Temkin-Pyzhev equation	$\xi_{A1}=\left(\dfrac{p_{NH_3}^2}{p_{H_2}^3}\right)^{\beta_{A1}}$	$K_{eq,j}$	Equilibrium constant for gas phase reaction j
	Steam inhibition	$\lambda_{A1}=\left(1+K_S p_{H_2O}\right)^{\alpha_{A1}}$	$K_{ads,i}$	Adsorption equilibrium constant for species i on reforming side
			β_{A1}	Dry ammonia kinetic exponent

	Mass action law methane/biogas (ammonia)	$R_{CH_4} = -r_{M1} - r_{M3} - r_{B1}$ (0) $R_{CO} = r_{M1} + r_{M2} + 2r_{B1}$ (0) $R_{CO_2} = r_{M1} + r_{M2} + r_{M3} - r_{B1}$ (0) $R_{H_2} = 3r_{M1} + r_{M2} + 4r_{M3} + 2r_{B1}$ ($3r_{A1}$) $R_{H_2O} = -r_{M1} - r_{M2} - 2r_{M3}$ (0) $R_{NH_3} = 0$ ($-2r_{A1}$) $R_{N_2} = 0$ (r_{A1})	α_{A1}	Aqueous ammonia steam inhibition exponent
			K_S	Aqueous ammonia steam inhibition coefficient
Current distribution	Ohm's law in 3D domains	$\nabla \cdot \mathbf{i}_v = Q_v$ $\mathbf{i}_v = -\sigma_v \nabla \Phi_v$	$\mathbf{i}_{v(s)}$	Volumetric (surface tangential) current density vector
	Ohm's law in 2D electrodes	$\nabla_T \cdot (d\mathbf{i}_s) = i_{mem}$ $\mathbf{i}_s = -\sigma_s \nabla_T \Phi_s$	Q_v	Volumetric current source
	Ohm's law (across membrane)	$\Delta\Phi_{mem} = \Phi_v - \Phi_s = ASR \cdot i_{mem} + E_{rev}$	$\sigma_{v(s)}$	Volumetric (surface in-plane) conductivity
			Φ	Electric potential
	Nernst equation	$E_{rev} = \dfrac{RT}{2F} \ln\left(\dfrac{p_{H_2,c}}{p_{H_2,a}}\right)$	d	Surface thickness
			$\Delta\Phi_{mem}$	Membrane cell voltage
	Membrane-electrode assembly normal resistance	$ASR = ASR^0 \exp\left(\dfrac{E_a}{R}\left(\dfrac{1}{T} - \dfrac{1}{1073K}\right)\right)$	E_{rev}	Reversible (Nernst) potential
			ASR	Area specific resistance
			$p_{H_2,c}$	H$_2$ partial pressure in cathode (sweep side)
			$p_{H_2,a}$	H$_2$ partial pressure in anode (reforming/decomposition side)
Heat transfer	Heat balance equation	$\rho C_p \mathbf{u} \cdot \nabla T + \nabla \cdot \mathbf{q} = Q_h$ $\mathbf{q} = -k\nabla T$	Q_h	Heat source
			$k_{(s)}$	Thermal conductivity (porous matrix solid fraction)
	Porous correction	$\mathbf{q} = -k_{eff}\nabla T$ $k_{eff} = \epsilon_p k + (1 - \epsilon_p)k_s$	$C_{p,i}$	Heat capacity at constant pressure of species i
	Gas mixture heat capacity	$C_p = \Sigma_i x_i C_{p,i}$	$Q_{h.j}$	Heat source from reaction j
	Heat sources	$Q_{h,j} = \Delta H_j r_j$ $Q_b = (ASR \cdot i_{mem} + E_{rev})i_{mem}$	ΔH_j	Enthalpy of reaction j
			Q_b	Boundary heat source from membrane
Property and material models	Wilke model (properties of gas mixtures)	$\eta = \displaystyle\sum_i \dfrac{x_i \eta_i}{\Sigma_j x_j \Psi_{i,j}}$ $\Psi_{i,j} = \dfrac{\left(1 + \left(\dfrac{\eta_i}{\eta_j}\right)^{\frac{1}{2}}\left(\dfrac{M_j}{M_i}\right)^{\frac{1}{4}}\right)^2}{\left(8\left(1 + \dfrac{M_i}{M_j}\right)\right)^{\frac{1}{2}}}$	η	Mixture property (viscosity, thermal conductivity)
			η_i	Temperature and pressure dependent property of species i
	Kozeny-Carman model (permeability)	$\kappa = \dfrac{d_p^2 \epsilon_p^3}{180(1 - \epsilon_p)^2}$	d_p	Porous media mean particle diameter
			v_i	Molecular diffusion volume for species i
	Fuller Schettler Giddings model (diffusivities)	$D_{ik} = \dfrac{1.01325 \cdot 10^{-2} T^{\frac{7}{4}}\left(\dfrac{1}{M_i} + \dfrac{1}{M_k}\right)^{\frac{1}{2}}}{p\left(v_i^{\frac{1}{3}} + v_k^{\frac{1}{3}}\right)^2}$		

Table S4.

Material specific properties used in multiphysics models.

Physics	Parameter	Symbol	Value	Unit
Fluid flow	Ni cermet porosity	ϵ_p	0.25	1
	Ni cermet mean particle diameter	d_p	1	µm
Chemical reaction kinetics	Nickel cermet BET specific surface area	A_{BET}	0.18	m^2/g_{cat}
	Kinetic parameters (table S5)			
Current distribution	Nominal ASR (800°C)	ASR^0	0.5	$\Omega \cdot cm^2$
	ASR activation energy	E_a	40	kJ/mol
	Conductivity, outer electrode (800°C)	σ_s	$8.8 \cdot 10^3$	S/cm
	Conductivity, inner electrode (800°C)	σ_v	$1.7 \cdot 10^3$	S/cm
	Conductivity, interconnect (800°C)	σ_v	$1.0 \cdot 10^3$	S/cm

Table S5.

Kinetic model parameters used in multiphysics models.

Reaction (j)	System	k_j^0 $(\text{mol} \cdot \text{m}_{\text{BET}}^{-2} \cdot \text{s}^{-1})$	$E_{a,j}$ $(\text{kJ} \cdot \text{mol}^{-1})$
M1	methane	$6.16 \cdot 10^{14}$	312
	biogas	$1.46 \cdot 10^{12}$	
M2	methane	$7.42 \cdot 10^{7}$	180
	biogas	$7.42 \cdot 10^{7}$	
M3	methane	$1.96 \cdot 10^{11}$	277
	biogas	$2.56 \cdot 10^{9}$	
B1	biogas	$1.98 \cdot 10^{5}$	118
A1	ammonia	$9.72 \cdot 10^{7}$	200
		$\beta_{A1} = 0.5 \,;\quad \alpha_{A1} = 4 \,;\quad K_S = 0.9$	

Table S6.

Equations for localized compression work of an isothermal and non-isothermal compression and separation process (Fig. 1B and fig. S1).

Model	Equation		Nomenclature
Governing equations	$\dfrac{dF_{H_2}}{dx} = -j_{H_2}^{mem}$	F_{H_2/N_2}	Molar flow rate of hydrogen/nitrogen (mol/s)
	$\dfrac{dF_{N_2}}{dx} = 0$	$j_{H_2}^{mem}$	Membrane flux per reactor length (mol/s)
		C_p	Heat capacity at constant pressure (J/(K·mol))
	$C_p(F_{H_2} + F_{N_2})\dfrac{dT}{dx} = \begin{cases} 0, & \text{isothermal} \\ \delta q(x), & \text{non-isothermal} \end{cases}$	T	Temperature (K)
	$\delta q(x) = \delta w(x) = RT\ln\left(\dfrac{p_{H_2}^{II}}{p_{H_2}^{I}(x)}\right) \cdot j_{H_2}^{mem}$	$\delta q(x)$	Localized heat of compression (J/mol)
		$\delta w(x)$	Localized compression work (J/mol)
Constraints	$F_{H_2}(x = 0) = 3F_{N_2}(x = 0)$	R	Universal gas constant (8.3145 J/(K·mol))
	$j_{H_2}^{mem} = \dfrac{F_{H_2}(x = 0)}{x = 1}$	$p_{H_2}^{II}$	Hydrogen pressure on permeate side (Pa)
	$p = \dfrac{RT}{\dot{v}}(F_{H_2} + F_{N_2}) = \text{const.}$	$p_{H_2}^{I}(x)$	Localized partial pressure of hydrogen on feed side (Pa)
		p	Total pressure (Pa)
		$\dot{v}$	Volumetric flow rate (m³/s)

References

18. H. Yokokawa, N. Sakai, T. Kawada, M. Dokiya, Thermodynamic Analysis of Reaction Profiles Between $LaMO_3$ (M = Ni , Co , Mn) and ZrO2. *J. Electrochem. Soc.* **138**, 2719-2727 (1991).

19. C. R. Wilke, A Viscosity Equation for Gas Mixtures. *J. Chem. Phys.* **18**, 517-519 (1950).

20. E. N. Fuller, P. D. Schettler, New method for prediction of binary gas-phase diffusion coefficients. *Ind. Eng. Chem.* **5**, 18-27 (1966).

21. J. Xu, G. F. Froment, in *AIChE J.* (1989), vol. 35, pp. 88-96.

22. C. A. Domenicali, F. A. Otter, Thermoelectric Power and Electrical Resistivity of Dilute Alloys of Silicon in Copper, Nickel, and Iron. *J. Appl. Phys.* **26**, 377-380 (1955).

23. R. A. Schapery, Thermal Expansion Coefficients of Composite Materials Based on Energy Principles. *J. Compos. Mater.* **2**, 380-404 (1968).

24. B. R. Powell, G. E. Youngblood, D. P. H. Hasselman, L. D. Bentsen, Effect of Thermal Expansion Mismatch on the Thermal Diffusivity of Glasì Ni Composites. *J. Am. Ceram. Soc.* **63**, 581-586 (1980).

25. H. An *et al.*, A 5×5 cm^2 protonic ceramic fuel cell with a power density of 1.3 W cm–2 at 600 °C. *Nat. Energy* **3**, 870-875 (2018).

26. VDM Metals. VDM Crofer 22H Specifications. (https://www.vdm-metals.com).

27. VDM Metals. VDM Crofer APU Specifications. (https://www.vdm-metals.com/).

28. A. Petric, H. Ling, Electrical conductivity and thermal expansion of spinels at elevated temperatures. *J. Am. Ceram. Soc.* **90**, 1515-1520 (2007).

29. Haynes International. HAYNES 242 allow Specifications. (https://www.haynesintl.com).

30. W. Z. Zhu, S. C. Deevi, Development of interconnect materials for solid oxide fuel cells. *Mater. Scie. Eng. A* **348**, 227-243 (2003).

31. O. Hodjati-Pugh, A. Dhir, R. Steinberger-Wilckens, The development of current collection in micro-tubular solid oxide fuel cells—a review. *Appl. Sci.* **11**, 1-27 (2021).

32. D. R. Ou, M. Cheng, X. L. Wang, Development of low-temperature sintered Mn-Co spinel coatings on Fe-Cr ferritic alloys for solid oxide fuel cell interconnect applications. *J. Power Sources* **236**, 200-206 (2013).

33. B. K. Park *et al.*, Cu- and Ni-doped $Mn_{1.5}Co_{1.5}O_4$ spinel coatings on metallic interconnects for solid oxide fuel cells. *Int. J. Hydrogen Energy* **38**, 12043-12050 (2013).

34. J. Xiao *et al.*, Oxidation of $MnCu_{0.5}Co_{1.5}O_4$ spinel coated SUS430 alloy interconnect in anode and cathode atmospheres for intermediate

temperature solid oxide fuel cell. *Int. J. Hydrogen Energy* **40**, 1868-1876 (2015).

35. S. P. Jiang *et al.*, Electrical conductivity and performance of doped LaCrO3 perovskite oxides for solid oxide fuel cells. *J. Power Sources* **176**, 82-89 (2008).
36. C. A. R. Board, "Low Carbon Fuel Standard - Annual Updates to Lookup Table Pathways," (2020).
37. M. Wei, S. V. Raghavan, P. Hidalgo-Gonzalez, "Building a Healthier and More Robust Future: 2050 Low-Carbon Energy Scenarios for California," *California Energy Commission* (2019).
38. C. A. R. Board, "Ethanol as a Transportation Fuel," (2017).
39. D. Kim *et al.*, paper presented at the 30th European Symposium on Computer Aided Process Engineering (ESCAPE30), 2020.
40. S. Roussanaly, A. L. Brunsvold, E. S. Hognes, Benchmarking of CO2 transport technologies: Part II - Offshore pipeline and shipping to an offshore site. *Int. J. Greenhouse Gas Control* **28**, 283-299 (2014).
41. A. Huss *et al.*, "JEC Tank-To-Wheels report v5: Passenger cars," (Joint Research Centre, 2020).